

Cyril Dosne<sup>1</sup>, Raphaël Barrier<sup>2</sup>, Sébastien Bourasseau<sup>1</sup>, Marco Carini<sup>2</sup>, Antoine Dumont<sup>2</sup> & Jacques Peter<sup>1</sup>

<sup>1</sup>DAAA, ONERA, Université de Paris Saclay, F-92322 Châtillon - France <sup>2</sup>DAAA, ONERA, Université de Paris Saclay, F-92190 Meudon - France

#### **Abstract**

The next generation of engine systems, such as ultra-high bypass-ratio engines or unducted fans, feature strong airframe-engine aerodynamic coupling phenomena. Similarly, new engine integration architectures, like Boundary-Layer Ingestion (BLI) or distributed propulsion systems lead to inlet distortions for the propulsive subsystem. These distortions can strongly alter the engine performance and operability limits, and are challenging to study in CFD because of their higher computational time and memory cost, when using classical blade-resolved simulations. Body-Force Modeling (BFM) methods have proven their capacity to faithfully reproduce both the engine performance trends and the distortion transfer across the successive blade rows, at a far lower cost than unsteady RANS (uRANS) simulations. The Hall body-force model presents a direct dependency to the fan blade shape parameters, with no mandatory prerequisite calibration, making it suitable for gradient-based optimizations. In previous studies, the adjoint formulation of this model has been implemented and validated. In this context, an evaluation of the body-force gradients accuracy under radial inlet distortion is first presented. Then, several optimizations are conducted to demonstrate those capabilities, and to identify the adjoint body-force limitations. This work will pave the way for the use of the adjoint body-force in highly coupled aero-propulsive optimizations of both the airframe and the engine geometries simultaneously.

Keywords: turbomachinery, distortion, optimization, body-force, adjoint, gradient-based

#### 1. Introduction

by 50% in 2050 relative to 2005 levels [1, 2, 3]. The forthcoming introduction of ultra-by-pass ratio engines, as well as the increasing attention towards unducted fan and new engine integration systems – such as distributed propulsion and boundary-layer ingestion – means that the future generation of aircraft engines will be subject to significant air intake distortions, for all or some operating conditions. For the engine subsystem, and especially for the fan, it implies being capable of performing blade shape optimization under distorted inlet conditions at early design stages. Eventually, a coupled modeling of the aerodynamics and propulsion subsystems will be required to maximize the aero-propulsive gains of these innovative configurations.

Such analysis requires engine modeling, especially at preliminary design stages. Indeed, even when considering a stationary azimuthal inlet distortion in the aircraft reference frame, the engine blades perceive a periodic forcing, which can lead to unsteady phenomena. To assess their effect on the overall aero-propulsive efficiency, conventional methods modeling the blade movement require an unsteady approach to analyze the distortion transfer across the engine. Since classical high-fidelity simulations as uRANS are cost prohibitive for preliminary optimization studies, propulsive models are required.

Many studies have been conducted to better understand the effects of an inlet distortion on the fan aerodynamics and on its performances. In that matter, BFM models have proven their ability to

faithfully reproduce the compressor performances as well as the distortion transfer across the blade rows [4, 5, 6], at far lower cost than their blade-resolved counterpart [7], and with higher level of fidelity than other throughflow models [8, 9]. As an example, López de Vega *et al.* [10] successfully used an explicit body-force model on a turbofan secondary airflow to analyze the effect of a BLI intake distortion on the overall turbofan efficiency. However, these BFM models are not yet widespread in the scientific community, and still lack an adjoint formulation to enable cost-efficient gradient-based optimization of compressors subject to inlet distortions.

Thus, only a few recent studies have focused on optimizing the fan design under inlet distortions, and most of them rely on blade-resolved simulations of the isolated compressor stage. In 2020, Da *et al.* [11] performed a compressor optimization through full annulus RANS simulations, using a genetic optimization algorithm. In order to perform steady simulations in the relative frame of reference, the authors made the distortion rotate with the rotor. The same year, Kumar, Turner and Celestina [12] undertook the optimization of a non-axisymmetric transonic IGV stage for tail-mounted BLI engines to damp the BLI inlet distortion at the fan face, once again with a genetic algorithm. The authors implemented a multi-fidelity design optimization. First, they undertook a cost-effective predesign relying on meanline methods to generate an initial geometry of the compressor blades, using a circumferential average of the inlet distortion as radial inlet conditions. Like Da *et al.*, the authors made use of steady RANS simulations during the optimization process, restricting the simulation to the IGV stage only to consistently perform a steady computation. As a result, no IGV-fan interaction could be captured. The inclusion of the rotor in the design process would again require expensive uRANS simulations, as suggested by the authors.

Alternatively, Godard et al. [7] used a body-force model, the Hall-Thollet model [13, 14], to perform full-annulus design optimization of a turbofan under a circumferential inlet distortion. After demonstrating the capability of this BFM model to reproduce the baseline performances and the distortion transfer through the fan-OGV stage using a steady CFD computation, the authors built-up a response surface of the compressor key performances, using the BFM. The lack of an adjoint formulation of the BFM prevented the authors from performing directly a gradient-based optimization of the compressor, which would have been more computationally efficient, and led them to build a metamodel. Nevertheless, their results suggest that the Hall-Thollet model is able of capturing the trends of the compressor performances and, once properly differentiated, should prove capable of driving a gradient-based optimization of a compressor under inlet distortion. In a recent work [15], we successfully implemented and validated the adjoint formulation of a simplified version of the Hall-Thollet model. Under clean inflow conditions, we showed that the gradients of the key compressor metrics with respect to rotor shape parameters can be faithfully reproduced by the Adjoint Body-Force Modeling (ABFM), over a large part of the engine characteristic, when compared to blade-resolved gradient evaluations. These results suggested the ABFM may provide blade shape gradients of the correct sign and amplitude under inlet distortions, and therefore may be used to perform preliminary compressor optimization under inlet distortions.

In this context, the goal of this paper is to investigate the opportunity of using the ABFM to improve the design of an axial compressor subject to inlet distortions, through various adjoint-based blade shape optimizations. First, a short reminder of the body-force methodology, the considered body-force model and the chosen compressor test case is presented. Second, a first evaluation of the body-force gradients accuracy under radial inlet distortion is carried out for several operating conditions. Third, gradient-based optimizations of this configuration are undertaken under radial inlet distortion, and the optimal design performances are assessed through blade-resolved simulations and compared to the baseline.

## 2. Test case settings

## 2.1 Recall of the BFM and ABFM methodologies

The BFM methodology consists in simulating the effect of the blades on the engine flow through source terms added to the right-hand side of the RANS equations, as proposed by Marble in 1964 [16]. The forcing of the flux balance is summarized in eq. (1), denoting by X the CFD mesh, W the corresponding discretized flow solution, S the body-force source terms, R the residual vector of the

discretized RANS equations and  $\tilde{R}$  its augmented form including body-force source terms:

$$R(\mathbf{X}, W) - S = \tilde{R}(\mathbf{X}, W, S) = 0. \tag{1}$$

As well illustrated in [7], the forces applied to the flow are modeled for each engine row, and blades are not meshed. Therefore, the BFM mesh is far simpler and smaller in size than its blade-resolved counterpart, thus reducing the memory and CPU wallclock-time needed to undertake the simulation. In addition, a BFM simulation does not require any complex interface condition between rotor and stator blade rows, such as mixing plane or sliding-mesh techniques. More importantly, the body-force computation can remain stationary even under inlet distortions. As a result, a BFM simulation requires less computational resources and engineer time to be set up than a blade-resolved one, and is undertaken with a far shorter computational time.

The BFM source terms are built upon a body-force  $\overrightarrow{f}$ , and various methods have been proposed in the literature to model this force, based on Marble's body-force decomposition [16]. Considering the absence of a blade metal blockage modeling and neglecting any contribution to the turbulence model, the general expression of S is given by

$$S = \left\{ \begin{array}{c} S_{\rho} \\ \overline{S_{\rho \nu}} \\ S_{\rho E} \\ S_{\tilde{\nu}} \end{array} \right\} = \left\{ \begin{array}{c} 0 \\ \rho \overrightarrow{f} \\ \rho \Omega r \overrightarrow{f} \cdot \overrightarrow{e_{\theta}} \end{array} \right\} , \tag{2}$$

where  $\Omega$  stands for the blade rotational speed, r is the radial distance to the rotational axis and  $\rho$  stands for the local flow density. Explicit methods intend to analytically evaluate  $\overrightarrow{f}$ , based on the local flow variables W and the engine parameters  $\beta$ .  $\beta$  can designate either operating parameters, such as the rotational speed of a given blade wheel, as well as blade shape parameters, such as the value of a local camber parameter. Consequently, the functional dependencies of the source terms can be expressed as  $S = S(X, W, \beta)$ . Because of their direct dependency to engine design parameters, explicit models, like the Hall-Thollet model [13, 14] are of high interest for blade shape optimizations [7].

In previous studies, a framework for explicit body-force models and for their adjoint formulation was implemented and validated. Details on the adjoint body-force formulation can be found in [17] and in [15]. Considering a Quantity of Interest (QoI)  $\mathcal{J}(X,W,\beta)$ , the adjoint body-force code implemented in [17, 15] gives access to the solution  $\tilde{\Lambda}$  of the adjoint equations taking into account the volume on the RANS residuals. The total gradient of  $\mathcal{J}$  with respect to a blade shape parameter reads:

$$\frac{d\mathcal{J}}{d\beta} = \underbrace{\left(\frac{\partial \mathcal{J}}{\partial \mathbf{X}} + \tilde{\Lambda}^T \frac{\partial \tilde{R}}{\partial \mathbf{X}}\right) \frac{d\mathbf{X}}{d\beta}}_{\text{BFM mesh}} + \underbrace{\left(\frac{\partial \mathcal{J}}{\partial \beta} + \tilde{\Lambda}^T \frac{\partial \tilde{R}}{\partial \beta}\right)}_{\text{BFM direct sensitivities}}.$$
 (3)

If one considers an engine parameter  $\beta$  affecting only the input fields of the body-force model, then only the direct BFM sensitivities in equation (3) contribute to the gradient. This is the case, for instance, for the rotor rotational speed  $\Omega$ . On the contrary, blade shape parameters – like the blade chord – can affect the blade camber-surface meridional projection, and therefore require a deformation of the blade-fitted body-force mesh. As consequences, both components of eq. (3) must be considered in the total gradient expression of  $\mathcal J$  with respect to  $\beta$ . Details on the gradient assembly, on the body-force pre-processing methodology and on the body-force mesh deformation process can be found in [15].

## 2.2 The considered body-force model

A simplified version of the Hall-Thollet model [13, 14] is considered here, with a loss model scaling quadratically with the angle  $\delta$  between the local flow velocity vector in the rotating reference frame  $\vec{v}$  and the blade camber surface, as schematized in Figure 1. All calibration coefficients were removed and no blockage model, compressibility correction or viscous loss model have yet been added. Our previous study [15] showed that this reduced version of the Hall-Thollet model provides a good

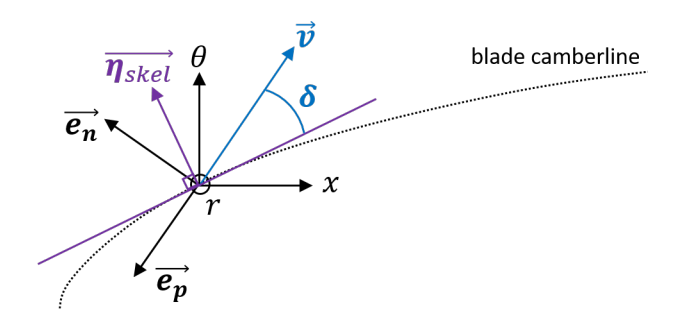


Figure 1 – 2D schematic of the unitary vectors used for the blade force decomposition regarding the blade camberline and the local flow deflection.

approximation of the time-averaged engine flow quantities and performance, as expected from the studies conducted by Thollet [14] and Godard [18]. The implementation of the body-force model, as well as of the QoIs and their respective adjoint formulation, was undertaken in an in-house ABFM library called BACARDI [17]. This library is interfaced with the modernized module [19] of the elsA software [20] (ONERA-Safran property). More details on the considered model, on its implementation and its adjoint formulation validation can be found in [15].

The body-force  $\overrightarrow{f}$  is expressed in the cylindrical coordinate system  $(\overrightarrow{e_x}, \overrightarrow{e_\theta}, \overrightarrow{e_r})$  associated to a blade row rotating around its axis  $\overrightarrow{e_x}$ , in the rotating frame of reference. Based on Marble's decomposition [16], f can be split in two contributions regarding the local relative flow velocity vector  $\vec{v}$ . The first, denoted  $\overrightarrow{f_p}$ , is parallel and opposite to  $\overrightarrow{v}$ , along the unitary vector  $\overrightarrow{e_p}$ . The second, denoted as  $\overrightarrow{f_n}$ , is normal to both  $\overrightarrow{v}$  and  $\overrightarrow{e_r}$  and oriented along the unitary vector  $\overrightarrow{e_n} = \overrightarrow{e_p} \wedge \overrightarrow{e_r}$ , with  $\wedge$  the vectorial product.

$$\overrightarrow{e_p} = -\frac{\overrightarrow{v}}{\|\overrightarrow{v}\|},$$
 (4)

and 
$$\overrightarrow{f} = \overrightarrow{f_n} + \overrightarrow{f_p} = f_n \overrightarrow{e_n} + f_p \overrightarrow{e_p}$$
. (5)

We denote by  $\overrightarrow{\eta_{skel}}$  the unitary vector normal to the blade camber-surface – chosen so that for a flat plate without pitch  $\overrightarrow{\eta_{skel}} = \overrightarrow{e_{\theta}}$  – and by  $\delta$  the local flow deviation, defined as the oriented angle between the plane locally tangent to the blade surface and  $\vec{v}$ . Thus, we define the unitary vector  $\overrightarrow{e_n}$  and the flow velocity component tangent to the camber-surface  $\overrightarrow{v_t}$  as follows:

$$\overrightarrow{v_t} = \overrightarrow{v} - (\overrightarrow{v} \cdot \overrightarrow{\eta_{skel}}) \overrightarrow{\eta_{skel}},$$
 (6)

$$\overrightarrow{v_t} = \overrightarrow{v} - (\overrightarrow{v} \cdot \overrightarrow{\eta_{skel}}) \overrightarrow{\eta_{skel}},$$
and  $\overrightarrow{e_n} = \cos(\delta) \overrightarrow{\eta_{skel}} - \sin(\delta) \frac{\overrightarrow{v_t}}{\|\overrightarrow{v_t}\|}.$ 
(6)

These unitary vectors are schematized in Figure 1.

The considered model, denoted as Quadratic Not Calibrated and derived from the Hall-Thollet model, is given by the following expressions:

$$f_n = \frac{1}{2} \|\overrightarrow{v}\|^2 2\pi \frac{\delta}{H \|\overrightarrow{\eta_{skel}} \cdot \overrightarrow{e_{\theta}}\|}, \qquad (8)$$

$$f_{n} = \frac{1}{2} \|\overrightarrow{v}\|^{2} 2\pi \frac{\delta}{H \|\overrightarrow{\eta_{skel}} \cdot \overrightarrow{e_{\theta}}\|},$$

$$f_{p} = 2\pi \delta^{2} * \frac{\|\overrightarrow{v}\|^{2}}{2H \|\overrightarrow{\eta_{skel}} \cdot \overrightarrow{e_{\theta}}\|},$$
(8)

where H stands for the distance between two consecutive blade camber surfaces, i.e.,  $\frac{2\pi r}{N}$  with Nthe number of blades.

The inputs of this body-force model, denoted Hall-QNC in the rest of this document, are for each blade wheel:

- its rotational speed  $\Omega_{RFM}$ ,
- its total number of blades N,

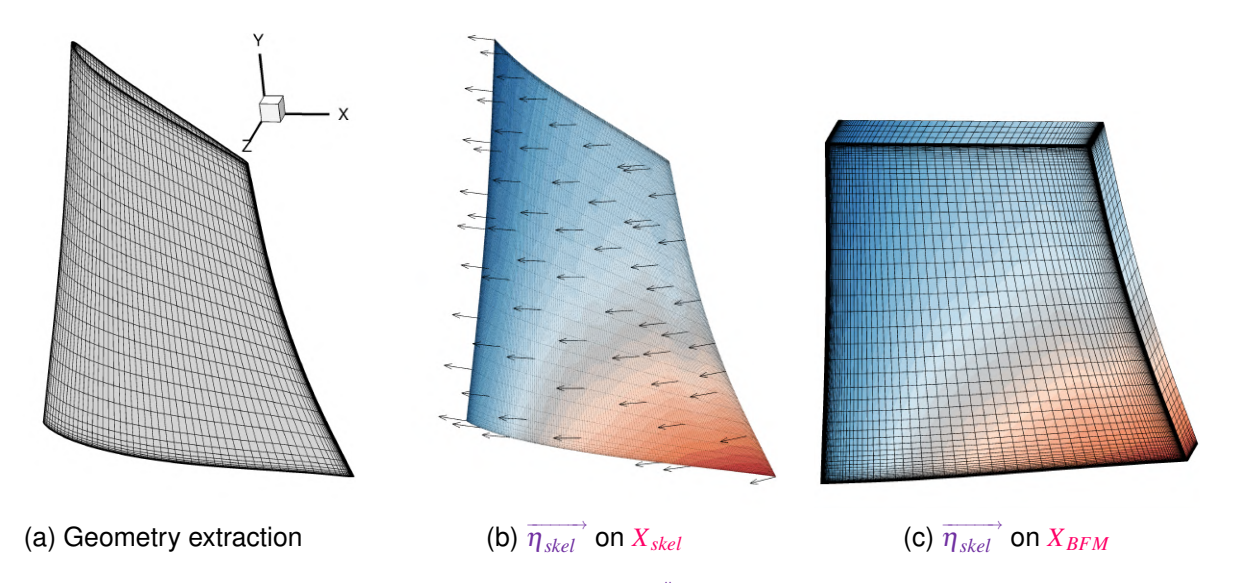


Figure 2 – Illustration of the process to generate the  $\beta_{X_{BFM}}^{\#}$  body-force input fields. (a) Blade skin extraction from the blade-resolved mesh; (b)  $\overline{\eta_{skel}}$  computation on the blade skeleton mesh  $X_{skel}$ . In this figure, the  $\eta_{skel_{\theta}}$  component field is depicted over the  $X_{skel}$  mesh; (c)  $\overline{\eta_{skel}}$  interpolated on the three-dimensional body-force mesh  $X_{BFM}$ . In this figure, the  $\eta_{skel_{\theta}}$  component field interpolated from  $X_{skel}$  to  $X_{BFM}$  is depicted.

• the component fields of the normal to the blade camber surface (or skeleton)  $\overrightarrow{\eta_{skel}}$  in the cylindrical coordinate systems, denoted  $\eta_{skel_x}$ ,  $\eta_{skel_\theta}$  and  $\eta_{skel_r}$ , respectively.

In the general case, these input fields are the result of the body-force pre-processing, which takes the engine design parameters  $\beta$ , the body-force mesh  $X_{BFM}$  and the mesh with discretized blade geometries (or blade-resolved mesh) as inputs. The process takes the blade-resolved mesh, depicted in Figure 2a, analyzes it and computes the camber surface of each blade row, using the ONERA's inhouse blade parametrization tool *ersatZ*. Then, the normal field is computed on this camber surface, as depicted in Figure 2b. It is finally interpolated from the blade skeleton surface to the 3D body-force mesh. In that process, depicted in Figure 2c, the body-force mesh  $X_{BFM}$  fits the edges of the blade skeleton projection on the meridional plane. We will designate it as a blade-fitted body-force mesh. For  $\Omega_{BFM}$  and N, the body-force variable  $\beta$  is a scalar duplicated in each cells of the mesh of the given row to store the value required by the body-force model.

### 2.3 The CME2 low-speed axial compressor

In this study, in order to provide a first assessment of the interest of the ABFM to conduct compressor shape optimization under inlet distortion, it was decided to use the same compressor configuration than in our previous study under clean inflow conditions (see [15]), on which the validation of the Hall-QNC adjoint code was undertaken. The CME2 compressor, which test bench is situated at Arts et Métiers in Lille, France, represents a high-pressure compressor stage, and has been extensively studied in recent years, both experimentally and numerically [21, 22]. In addition to the high experience ONERA has accumulated on this test case, this compressor geometry is a good subject for a preliminary investigation of the Hall-QNC model, as it does not show pronounced compressible phenomena that would necessitate the implementation of additional modeling components in the body-force model. The compressor is comprised of two rows of blades: the rotor has 30 blades while the stator has 40 blades. Figures 4a and 4b presents the blade-resolved single blade-passage mesh and its body-force counterpart, respectively. A meridional schematic of the CME2 channel is also given in Figure 4c, where post-processing stations later used are drawn in turquoise. The body-force mesh is generated from its blade-resolved counterpart and features a cell size of  $10^{-6}$  m at the walls and of  $10^{-5}$  m at the rows leading and trailing edges (see [15] for details on the blade-fitted BFM mesh generation). The blade-fitted BFM mesh features approximately 1.4 10<sup>5</sup> cells and is treated as unstructured, while the blade-resolved structured mesh features approximately 1.22 10<sup>6</sup> cells. A mixing plane condition is used at the rotor-stator interface.

In this study, reference quantities remain unchanged and feature a total temperature  $T_{t_0} = 288.15$  K and a total pressure  $P_{t_0} = 101325$  Pa. We consider a radial inlet distortion featuring a 5% total pressure loss at the hub, compared to the reference total pressure imposed at the shroud. The total pressure map imposed on the inlet is shown in Figure 3. All other quantities, i.e. the total enthalpy, the inlet flow direction and the turbulence variable, are imposed as uniform at the inlet and equal to the reference state values. The rotation speed considered here is 6400 RPM, very close to the compressor design

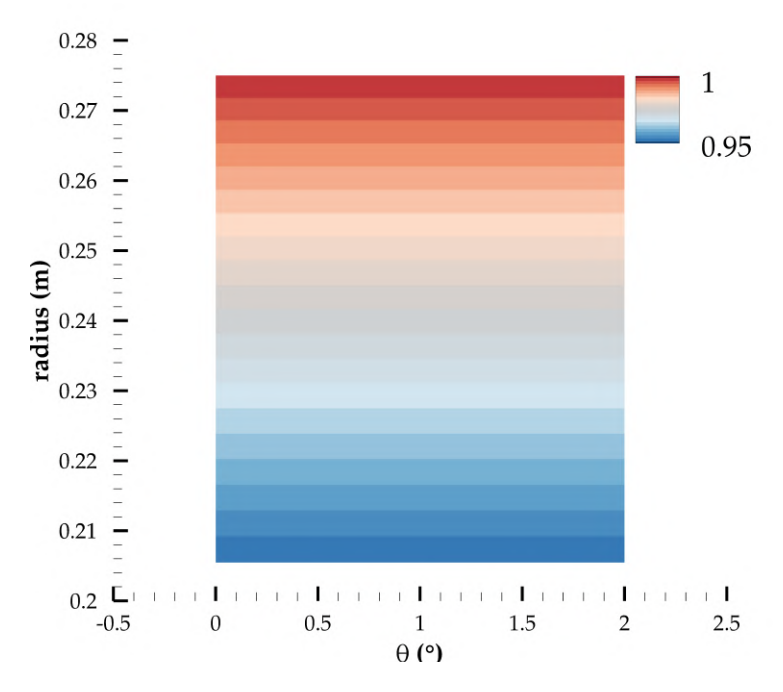


Figure 3 – Map of the total pressure inlet distortion for the body-force simulation, made non dimensional by the reference total pressure  $P_{t_0}$ .

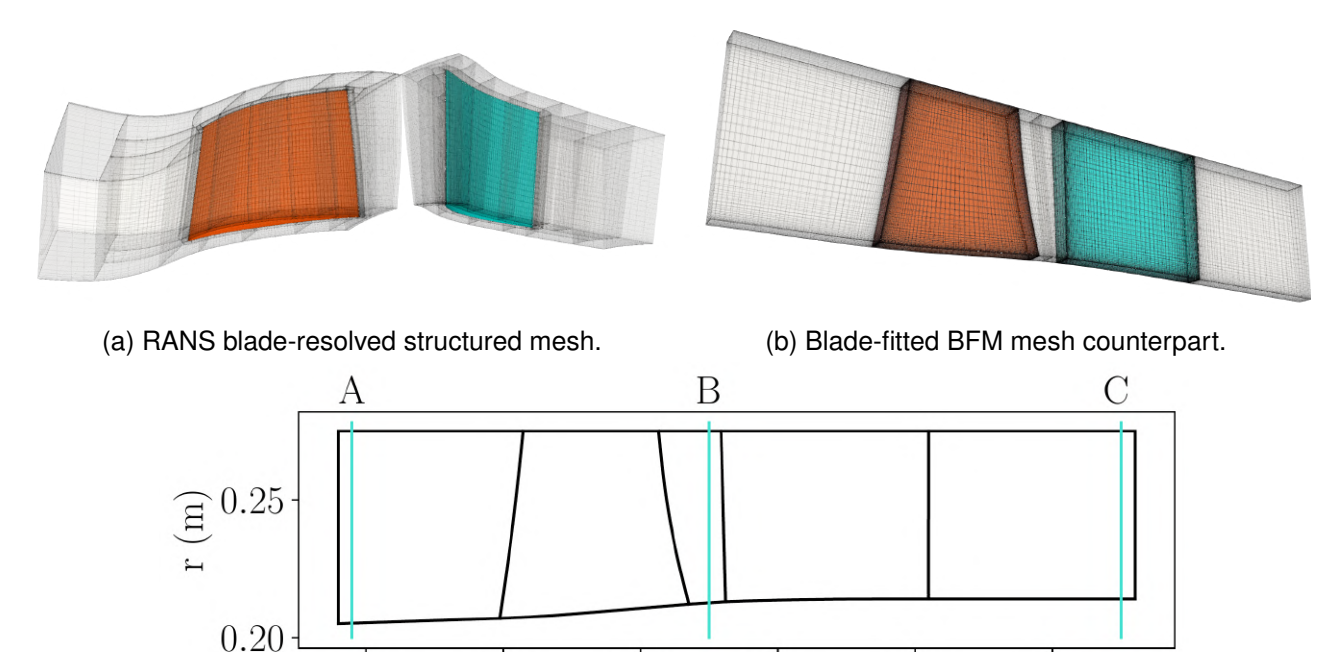
speed. Viscous wall boundary conditions are imposed at the hub and shroud. Periodic boundary conditions are imposed at the sides of the channel. In this test case, the Spalart-Allmaras (SA) turbulence model was employed, with its negative formulation for the body-force simulations [23], and with the QCR correction for the blade-resolved simulations [24]. The convective fluxes are discretized using the Roe scheme [25]. The discrete viscous fluxes are computed based on cell-centered gradients corrected at the interface in the direction of the two adjacent centers. Studies on the blade-resolved mesh are carried out using the 'legacy' modules of *elsA* [20], while the body-force computations are performed using the modernized module of *elsA* [19].

# 3. BFM accuracy under inlet distortions

#### 3.1 Compressor characteristic under radial inlet distortions

The engine characteristics under this radial inlet distortion are calculated for both the Hall-QNC body-force model and the blade-resolved case. The engine characteristics obtained under the radial inlet distortion with the Hall-QNC model – in dashed lines – and with the blade-resolved simulations – in plain lines – are drawn in black in Figure 5. The results obtained under clean inflow conditions are also presented in blue for comparison. The objective of this comparative study is to assess the capacity of the Hall-QNC model to reproduce the alterations in compressor performances resulting from inlet distortion.

It can be observed that the body-force model correctly captures the reduction of the choke massflow-rate, the increase of the stability limit massflow-rate, and the reduction of both the compressor efficiency  $\eta$  and static pressure ratio of the whole stage  $\Pi_{P_s}$  due to the inlet distortion. The loss overestimation and tendency errors observed under clean inflow inlet conditions (detailed in [15]), mainly near the blockage, for this model are not significantly increased by the presence of the radial inlet distortion. The blade-resolved characteristic under inlet distortions shows a decrease of 1.7%



(c) Meridional view of the CME2 channel with post-processing stations

0.10

x(m)

0.15

0.20

0.05

-0.05

0.00

Figure 4 – Geometry of the CME2 single blade passage channel and its associated RANS (a) and BFM (b) meshes. The rotor geometry is colored in orange, and the stator in cyan. The body-force blocks fitting the blade edges projected on the meridian plane are represented using the same colors; (c) Meridional view of the CME2 channel, with the position of the post-processing stations used in all following studies.

of the choke massflow-rate and a 4.5% drop of the efficiency at  $\dot{m}\approx 12 {\rm kg.s^{-1}}$  compared to the results obtained under clean inflow conditions. As a comparison, the Hall-QNC model predicts a 3.5% drop of the maximum efficiency at  $\dot{m}\approx 12 {\rm kg.s^{-1}}$ , and a 2.7% decrease of the choke massflow-rate. As observed under clean inflow condition, this body-force model is capable of reproducing the compressor performance trends even at low massflow-rates, even if does not correctly capture the blockage and overestimates the losses. These results therefore show that this model also performs well under moderate radial inlet distortion.

To provide further insight, the meridional slice of the body-force simulation is compared to the circumferential average of the blade-resolved flow solution, under radial inlet distortion at  $\dot{m} = 12.0 \, \text{kg.s}^{-1}$ . The comparison of meridional contours is given in Figure 6. Especially, radial velocity contours in the absolute reference frame are given, since significant radial flow redistribution is observed on the rotor due to the radial inlet distortion. Comparing the total pressure contours of Figures 6b and 6a, it appears once again that the Hall-QNC model correctly reproduces the total pressure distribution over the channel, even if it still underestimates the mechanical energy transferred to the flow. In particular, the body-force does not properly capture the high blade work at the rotor root. However, it correctly reproduces the total pressure losses on the stator, especially in the lower half part of the channel. Comparing the total temperature contours of Figures 6d and 6c demonstrates once again the accurate modelization of the power transferred by the blade to the flow using the Hall-QNC model. Finally, the comparison of the radial component of the flow velocity in the absolute reference frame, given in Figures 6f and 6e, shows that the BFM proves capable of capturing at some extent the radial flow redistribution on the rotor row, even if contour levels are underestimated near the endwall and especially near the hub. The body-force model also predicts a significant negative radial velocity at the stator leading edge that is not observed on the blade-resolved circumferential average. Thus, the body-force modeling accuracy appears reduced on the stator row.

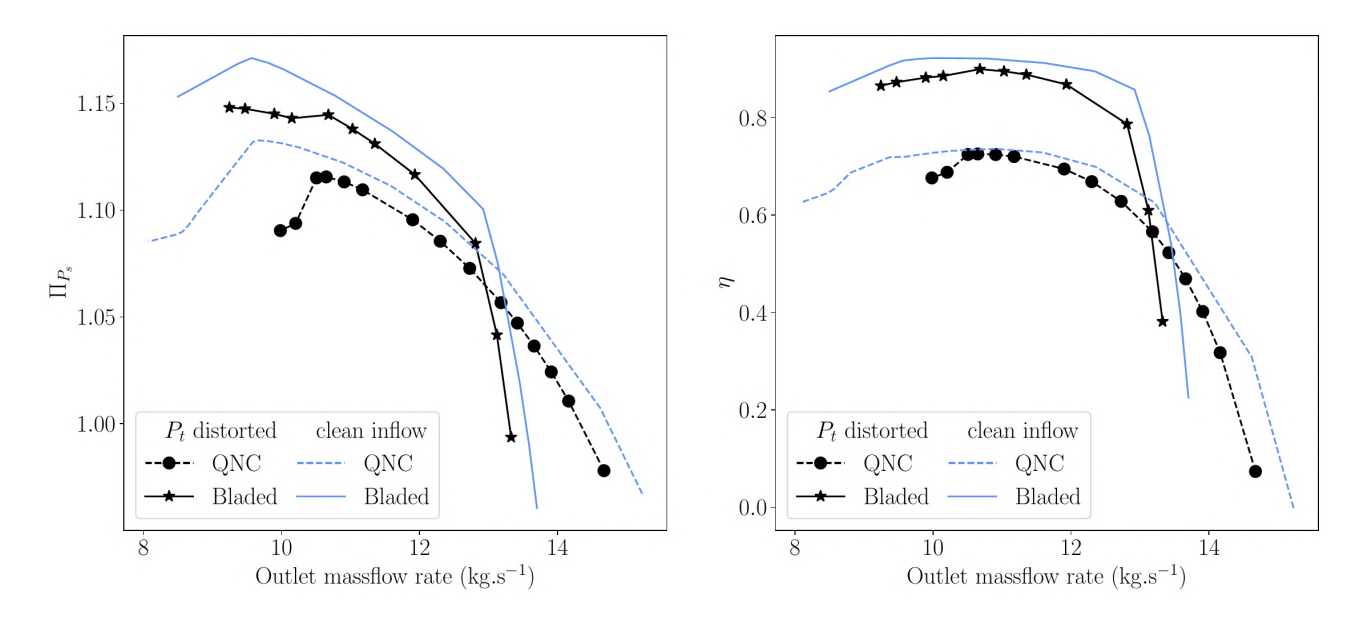


Figure 5 – Engine characteristics at 6400 RPM, in black for the results obtained with the SA-QCR turbulence model under radial inlet distortions, and in blue for the results obtained with the SA model under clean inflow conditions. Blade-resolved results are drawn in plain lines, those obtained with the BFM model are drawn in dotted lines. Performances are evaluated through flow integrals at station A and C.

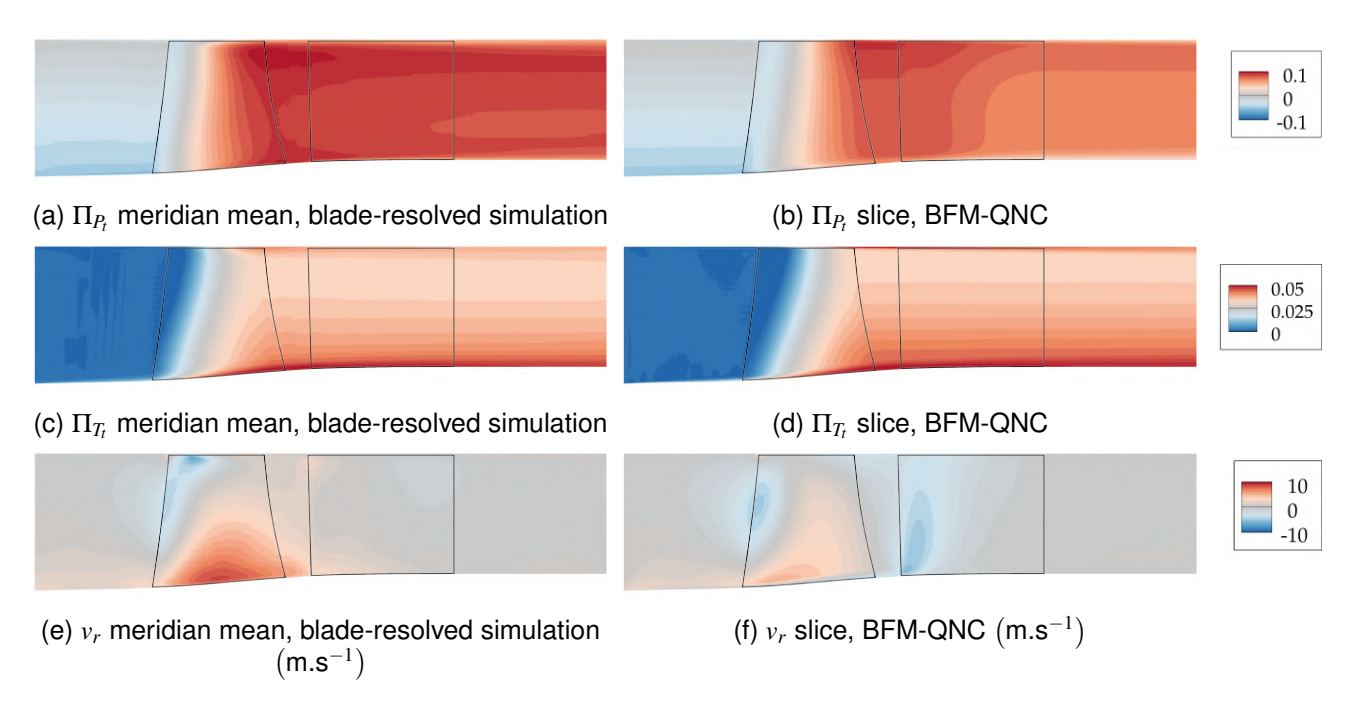


Figure 6 – Comparison between circumferential averages of the blade-resolved simulations (left) and BFM meridian slices (right) at  $\dot{m}=12\,\mathrm{kg.s^{-1}}$ . Contours of total pressure ratio (top row), total temperature ratio (middle row) and of radial velocity (bottom row) in the absolute reference frame. The meridional position of the blade edges are drawn in black.

## 3.2 Evaluation of the adjoint BFM gradient accuracy

The methodology for assessing the ABFM design capabilities under inlet distortions, as detailed in [15], is briefly recalled here. It is necessary to assess the physical relevance of the gradients of the typical compressor performance metrics (namely the power consumption, the total pressure ratio and the massflow-rate) predicted by the ABFM at several points along the compressor characteristic for a given rotating speed, especially near design conditions (i.e., in the stable part of the characteristic), near the stability limit and near the choke. Indeed, in addition to the reduction in power consumption targeted at a specific design condition, a typical compressor optimization often requires constraints at off-design operating conditions. For instance, this may to maintain constant the blockage massflow-rate. Furthermore, in the general case of a full-annulus inlet distortion, it has been observed that a given blade of the rotor describes an orbit on the characteristic as it is subjected to various inflow conditions [26]. In such a case, it is necessary (though not sufficient) that the blade shape sensitivities captured by the ABFM on a single blade passage under radial inlet distortions are relevant on a significant portion of the compressor characteristic in order to properly capture the blade shape sensitivities on a full-annulus case with, for instance, a BLI-like inlet distortion.

To perform this evaluation, ABFM gradients must be compared to their blade-resolved counterparts, using the same single blade-passage configuration as previously. Due to the necessity of performing numerous gradient evaluations, the blade-resolved gradients are evaluated with the *elsA* adjoint capabilities. In the subsequent gradient comparison, these adjoint blade-resolved gradients are used as a reference to assess the physical representativeness of the ABFM gradients. Nevertheless, a few finite-difference studies were conducted to evaluate the numerical accuracy of the SA-QCR adjoint capability recently implemented in *elsA*. For the ABFM, the validation of the gradients was undertaken on the same configuration at the same rotating speed in [15], with adjoint gradients within 0.1% of the FD gradient evaluations.

We first evaluate the gradients of the compressor power consumption  $(Q_{POW})$  with respect to the camber control points placed over the rotor and stator camber-surfaces, as depicted in Figure 7. The body-force mesh deformation cannot yet cope with strong displacements near the hub and the shroud so the control point values at the hub and the shroud are forced at 0 to avoid any mesh displacements near the walls. The camber control point values at the stator trailing edge are also forced to zero. These zero-deformation control points are depicted in gray. The control points for which the gradients are evaluated are placed at 10, 25, 50, 75 and 90% of the channel height h respectively, each channel height being identified by a different color. For 10 control points, bladeresolved finite-differences (FD) were conducted to assess the numerical accuracy of both the adjoint blade-resolved gradient evaluations and of the ABFM. The control points for which FD gradients were evaluated are identified with a thick black circle in Figure 7. A FD step study was conducted for four of these camber parameters and showed that the gradient values predicted were not highly sensitive to the choice of the step used on the blade shape parameters, i.e., 0.001° (this study is not shown in this paper). FD steps between  $0.001^{\circ}$  and  $0.1^{\circ}$  were tested with a maximum variation observed on the rotor gradients of 5% and most of them within 2% variation. For the stator, high variations of the FD gradients were observed with the FD step, thus no definitive conclusion can be drawn. They are displayed to discuss the further investigations that need to be undertaken, althought they cannot be considered as a reference. In addition, a significant mismatch between blade-resolved and FD gradients were observed for the stator control points. Despite some efforts undertaken to identify the sources of blade-resolved gradients inaccuracies and solve them, a strong uncertainty still persists on the blade-resolved stator gradients. Additional investigations are necessary to mitigate these discrepancies on this particular test case. In the meantime, only the FDs gradients are shown for the blade-resolved evaluations on the stator.

This gradient comparison is first undertaken at  $\dot{m}=12.0\,\mathrm{kg.s^{-1}}$ , so near the compressor design operating conditions. This comparison is depicted in Figure 8, where dot-filled bars correspond to the ABFM gradients and the squared bars correspond to the adjoint blade-resolved gradients. Finally, the blade-resolved finite-differences are drawn in beige bars. A good match between ABFM and

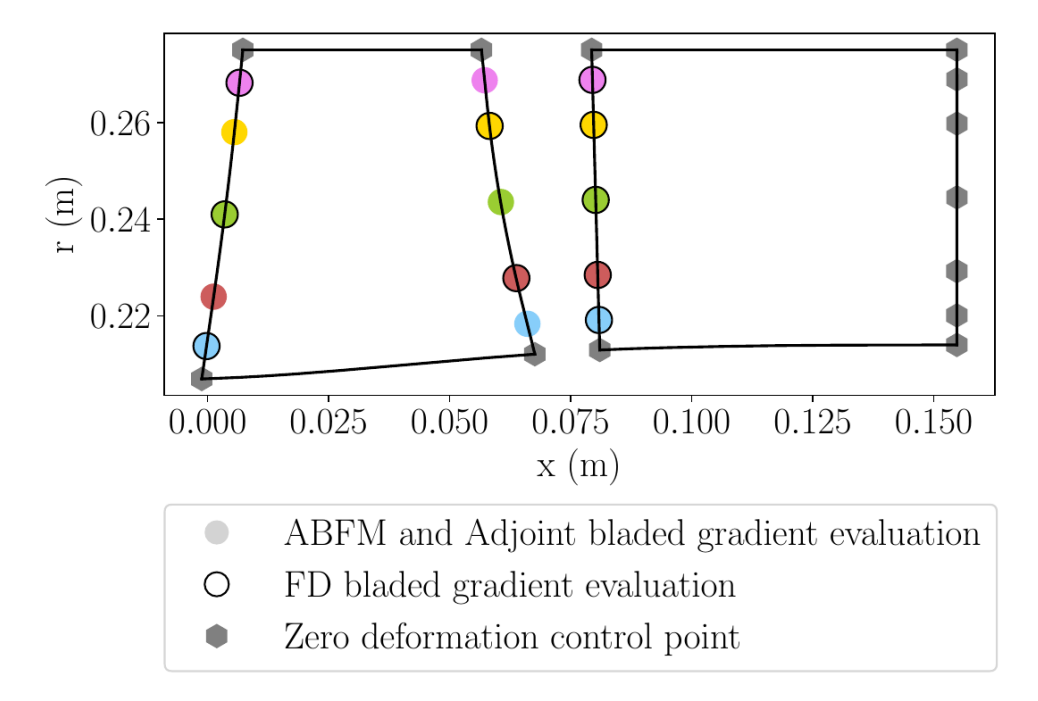


Figure 7 – Rotor and stator camber control points placed over the blade camber-surfaces for the gradient comparison between ABFM, adjoint blade-resolved and FD blade-resolved gradients.

adjoint blade-resolved gradients can be observed for all rotor camber parameters. The maximum error is observed at the leading edge for 25% channel height, the ABFM over-predicting the gradient by 34% compared to the blade-resolved reference. All other gradient relative differences are within 15% for the rotor. Both adjoint blade-resolved gradients and ABFM predictions are found consistent with the blade-resolved FD evaluations. However, FD results are often closer to the ABFM values than to the blade-resolved adjoint gradients. The relative difference between adjoint and FD blade-resolved gradients ranges between 8 and 25% for the rotor, the maximum error being observed at the leading edge for 10% channel height. This difference between blade-resolved gradients is higher than expected and further FD study is necessary to assess more precisely the accuracy of the adjoint blade-resolved gradients. Nevertheless, this gradient comparison demonstrates the capability of the Hall-QNC adjoint formulation to predict the  $\mathcal{Q}_{POW}$  rotor shape gradients under inlet distortion near design condition.

At a second time, an attempt was made to conduct the same gradient comparison for the stator was conducted, focusing on the leading edge gradients as these would be used as design variables in a stage shape optimization. These preliminary results are presented on the right-hand side of Figure 8. It can first be observed that the stator shape gradients are at least one order of magnitude lower than their rotor counterparts. Secondly, a significant discrepancy between the FD blade-resolved and the ABFM gradients can be observed. The two methods frequently yield gradients of very different amplitude. Given the variability observed in the FD gradients with the step applied on the camber parameters on the one hand, and the significant mismatch found between FD and adjoint blade-resolved gradients on the other hand, a rigorous gradient comparison for the stator cannot yet be drawn. Furthermore, the aforementioned uncertainties on the stator blade-resolved gradients have so far prevented the conduct of blade-resolved adjoint-based optimization of the CME2 compressor. Nevertheless, these preliminary results indicate that the ABFM may be capable of accurately predicting the sign and order of magnitude for the majority of stator shape gradients. However, further studies are required to confirm or refute this hypothesis.

As a final step of this gradient comparison, the same rotor shape gradient comparison was conducted for two other compressor performance metrics (the stage total pressure ratio  $Q_{\Pi_{P_i}}$  and massflow-rate  $Q_{\dot{m}}$ ) as well as for two other operating conditions (near stall  $\dot{m}=11.0 \, \mathrm{kg.s^{-1}}$  and near choke  $\dot{m}=13.0 \, \mathrm{kg.s^{-1}}$ ). A synthesis of the gradient comparison is given in Figure 9. To help discuss the ABFM gradient prediction accuracy, compared to their adjoint blade-resolved counterparts, several

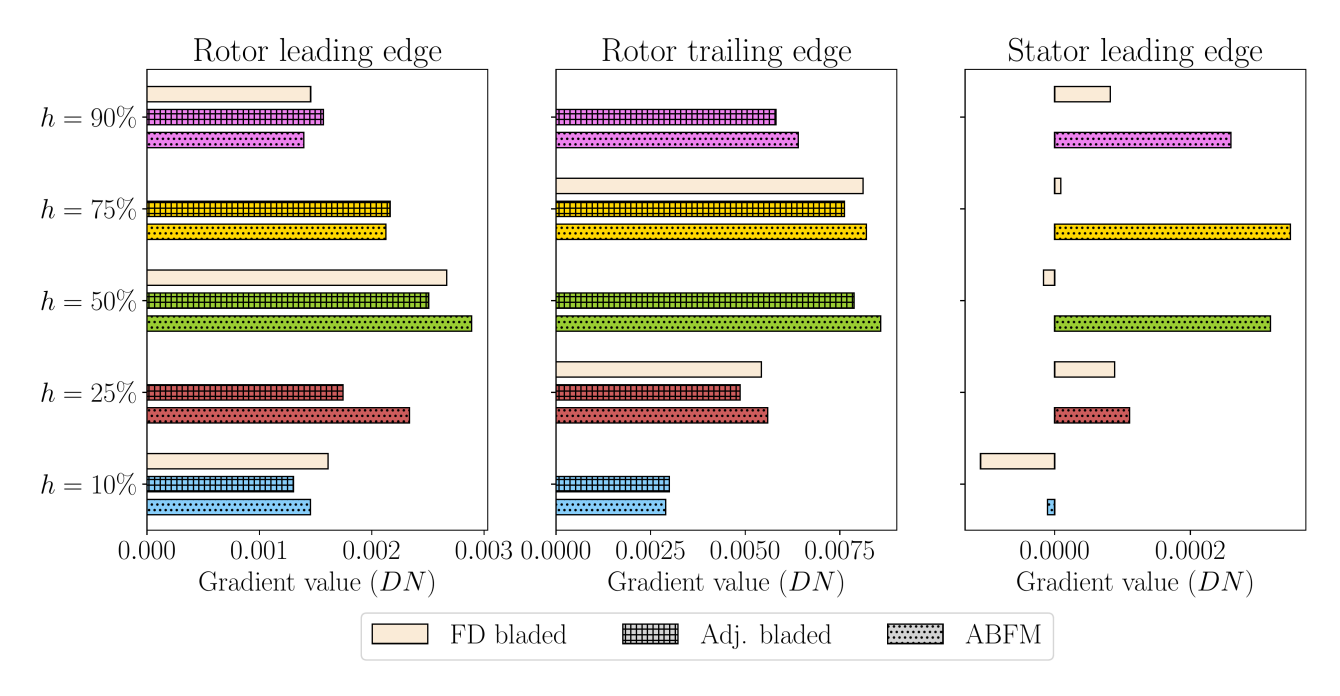


Figure 8 – Gradient comparison for the compressor power consumption with respect to the camber control points depicted in Figure 7 at  $\dot{m} = 12.0 \,\mathrm{kg.s^{-1}}$ .

#### error metrics are used:

•  $|\varepsilon_{max}|$  designates the maximum observed over the absolute values of the difference between ABFM and blade-resolved gradients, relative to the blade-resolved gradient value. It is given by the following equation:

$$|\varepsilon_{max}| = \max_{i \in [1,10]} \left| \frac{\nabla^{i}_{ABFM} - \nabla^{i}_{bladed}}{\nabla^{i}_{bladed}} \right|,$$
 (10)

with  $\nabla^i_{ABFM}$  the  $i^{th}$  rotor shape gradient of the considered QoI predicted by the ABFM and  $\nabla^i_{bladed}$  its adjoint blade-resolved counterpart.

- $|\varepsilon_{min}|$  designates similarly the minimum observed over the absolute values of the difference between ABFM and blade-resolved gradients, relative to the blade-resolved gradient value.
- $\varepsilon_{RMSE}$  denotes the Root Mean Square Error measured over the 10 relative differences between ABFM and adjoint blade-resolved gradients. It is given as follows:

$$\varepsilon_{RMSE} = \sqrt{\frac{1}{10} \sum_{i \in [1,10]} \left( \frac{\nabla_{ABFM}^{i} - \nabla_{bladed}^{i}}{\nabla_{bladed}^{i}} \right)^{2}} . \tag{11}$$

•  $\varepsilon_{\sigma}$  finally represents the standard deviation of the gradient relative differences over the 10 rotor shape gradients studied. Denoting by  $\Box$  the mean operand over the 10 gradient relative difference values, it is evaluated through the following equation:

$$\varepsilon_{\sigma} = \sqrt{\frac{1}{10} \sum_{i \in [1, 10]} \left( \frac{\nabla_{ABFM}^{i} - \nabla_{bladed}^{i}}{\nabla_{bladed}^{i}} - \overline{\left[ \frac{\nabla_{ABFM}^{i} - \nabla_{bladed}^{i}}{\nabla_{bladed}^{i}} \right]} \right)^{2}} . \tag{12}$$

These error metrics are suited to evaluate the physical representativeness of the ABFM blade shape gradients. Alternatively, the same error metrics can be evaluated based on a difference between ABFM and blade-resolved gradient values relative to the maximum of the blade-resolved gradient values observed, for a given QoI. These quantities are denoted with the superscript  $\bullet^{\mathcal{O}}$  and are

usefull to assess the representativeness of the ABFM gradients from the optimizer point of view, as the maximum gradient amplitude drives the descent direction. For instance,  $\varepsilon_{RMSE}^{\mathcal{O}}$  is given as follows:

$$\varepsilon_{RMSE}^{\mathcal{O}} = \sqrt{\frac{1}{10} \sum_{i \in [1, 10]} \left( \frac{\nabla_{ABFM}^{i} - \nabla_{bladed}^{i}}{\max_{i \in [1, 10]} \left| \nabla_{bladed}^{i} \right|} \right)^{2}} . \tag{13}$$

As observed in [15] for clean inflow conditions, a good gradient comparison is observed between ABFM and blade-resolved shape gradients for near design operating conditions as well as near the stability limit. Indeed, the ABFM is capable of predicting the  $\mathcal{Q}_{POW}$  gradients with a relative RMSE error within 14.6% and 10.6% respectively. For these two operating conditions, the standard deviation observed on the 10 relative differences between ABFM and blade-resolved gradients are also similar with  $\varepsilon_{\sigma}=12.4\%$  and 10.% respectively. The only significant difference is observed on the maximum relative difference observed, which reaches 33.9% near design conditions against only 16.7% near the stability limit.

As observed in our previous study under clean inflow conditions, a lower accuracy is observed for  $\mathcal{Q}_m$  and  $\mathcal{Q}_{\Pi_{P_1}}$  with  $\varepsilon_{RMSE} \approx 22\%$  and  $\varepsilon_\sigma \approx 23\%$  at the design massflow-rate. These predictions are slightly degraded near the stability limit ( $\varepsilon_{RMSE} \approx \varepsilon_{sigma} \approx 30\%$ ), and a noticeable increase of the maximum relative difference is observed. Leading edge gradients above 75% of the channel height were found responsible for this increase in error metrics, while the relative difference between ABFM and blade-resolved gradients were found to be reduced at the rotor trailing edge. Knowing that this compressor stage is tip-critical [27], this may be the sign that strong viscous phenomena are appearing at the blade leading edge, that cannot be captured by the BFM model currently used. Further analysis on this matter is needed.

Finally, the ABFM gradient accuracy is decreased near the blockage, mainly for  $\mathcal{Q}_{POW}$ . At  $\dot{m}=13\,\mathrm{kg.s^{-1}}$ ,  $\mathcal{Q}_{POW}$  gradients are predicted with a mean relative error  $\varepsilon_{RMSE}$  of 40.8%, the standard deviation reaches 43% and the maximum relative difference measured is nearly at 80% of the bladeresolved gradient value. On the contrary, for both  $\mathcal{Q}_{\dot{m}}$  and  $\mathcal{Q}_{\Pi_{P_i}}$  the ABFM gradient prediction accuracy is similar than near the stability limit, with  $\varepsilon_{RMSE}\approx30\%$ . At this operating conditions and for all three Qols, the ABFM prediction error is found maximal at high channel heights, especially near the leading edge. The same behaviour was observed under clean inflow conditions, and a flow separation at the rotor leading edge was found responsible for this decrease in ABFM gradient accuracy. Once again, a deeper analysis of the flow field is needed to ascertain these hypothesis.

Using the error metrics relative to the maximum gradient amplitude evaluated over the 10 rotor shape gradients, it can be observed that all ABFM gradients are within 25% and on average within  $\approx 10\%$  of the blade-resolved gradients at design conditions and near the stability limit. Near the blockage, the maximum relative differences remain high, but ABFM gradients are still predicted, on average, within  $\approx 30\%$ . Therefore, the ABFM is capable of providing the correct descent direction and gradient amplitude to an optimizer, even near the choke.

In conclusion, the ABFM is capable of accurately reproducing the  $\mathcal{Q}_{POW}$  gradients over a significant portion of the characteristic, as well as the  $\mathcal{Q}_m$  and  $\mathcal{Q}_{\Pi_{P_l}}$  gradients. However, these capabilities are diminished near blockage conditions, despite the ABFM ability to capture the correct sign and order of magnitude of all rotor shape gradients. Further modeling is needed to mitigate these limitations of the ABFM, such as introducing a blade metal blockage modeling into the BFM model, as proposed by Chima [28] or Kottapalli [29]. Nevertheless, the ABFM would most likely prove capable of reproducing the rotor shape gradients of the key compressor performance metrics quite accurately, even under full-annulus inlet distortion. In such a case, the reduced accuracy observed in the vicinity of the blockage may limit the ability of the optimizer to perform a rotor shape trade-off between the different operating conditions the blade experiences during its rotation. Still, the ABFM would most likely be able to provide the optimizer with the correct descent direction and gradient amplitude. Therefore, it would allow for efficient compressor design optimizations under inlet distortion. In the next section, the ABFM-driven compressor optimization is put to a test, again with the compressor subjected to

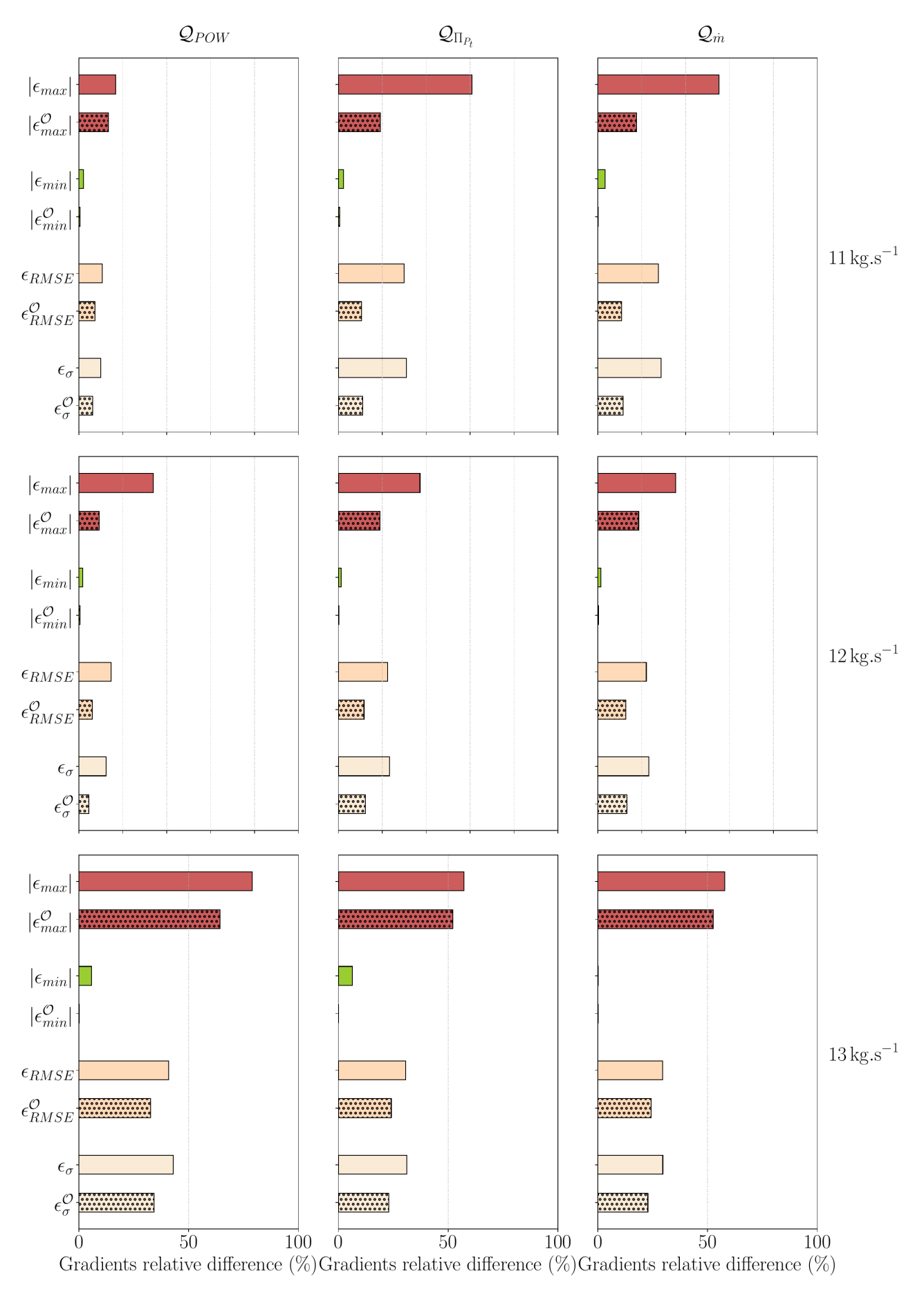


Figure 9 – Error metrics between ABFM and adjoint blade-resolved gradient evaluations for the three studied QoIs (columns) and the three studied operating conditions at  $\dot{m}=11,\,12$  and  $13\,\mathrm{kg.s^{-1}}$  (rows) for the rotor shape gradients. Dots-filled bars represent the error metrics relative to the maximum of the blade-resolyed gradient values observed.

a total pressure radial inlet distortion in order to allow for a fast blade-resolved evaluation of the performance of the optimized configuration.

## 4. ABFM for compressor design under inlet distortions

Previous results have demonstrated the ABFM ability to predict rotor shape gradients in presence of a radial inlet distortion of total pressure. They have also shown that compressor performances are significantly altered by this inlet distortion, despite its small amplitude. This section evaluates the potential of using the ABFM as a design tool to adapt, through gradient-based shape optimization, compressor configurations designed under clean inflow conditions to distorted ones, i.e., to design distortion-tolerant compressor stages. The rotor and stator shape parameterization used for the ABFM gradient study and depicted in Figure 7 is employed once again. The stage parameterization therefore features a total of 15 active camber control points.

The camber control points are designated as  $\beta_{hX,mY}^{row}$  with row representing either the rotor or the stator, hX denoting the relative channel height and mY the relative meridional position over the blade camber surface. The range within which the camber deformation parameters may vary during the optimization process is set to  $[-3.0^{\circ}\,;\,3.0^{\circ}]$ , since this range was observed to be safe to ensure a good quality of the deformed body-force mesh. The objective function to be minimize is the compressor power consumption  $\mathcal{Q}_{POW}$ , subject to an equality constraint on the massflow-rate  $\mathcal{Q}_m$  and an inequality constraint on the total pressure ratio  $\mathcal{Q}_{\Pi_{P_l}}$ . The first problem formulation, denoted  $\mathcal{T}$ , is therefore given as follows:

$$\begin{array}{ll} \text{minimize} & \mathcal{Q}_{POW\,a} \\ \text{subject to} & \beta_{h_x m_y}^{rotor} \in [-3.0\,;\,3.0] \text{ for } x \in [10,25,50,75,90] \text{ and } y \in [0,100] \\ & \beta_{h_x m_0}^{stator} \in [-3.0\,;\,3.0] \text{ for } x \in [10,25,50,75,90] \\ & \mathcal{Q}_{\dot{n}a} = 1.0 \\ & -\mathcal{Q}_{\Pi_{P_t}a} \leq -1.0 \\ \text{regarding} & \beta_{h_{10}m_0}^{rotor} \text{ to } \beta_{h_{90}m_{100}}^{rotor}, \text{ and } \beta_{h_{10}m_0}^{stator} \text{ to } \beta_{h_{90}m_0}^{stator} \\ \text{with the zero deformations} & \beta_{h_x m_{100}}^{stator} = 0.0 \text{ for } x \in [10,25,50,75,90] \\ & \beta_{h_x m_y}^{row} = 0.0 \text{ for } x \in [0,100], y \in [0,100] \text{ and } row \in \{rotor, stator\} \ , \end{array}$$

where  $ullet_a$  subscripts denotes the QoIs divided by their associated value on the baseline configuration. In addition, the rotor rotation speed  $\Omega$  can be considered as an additional design variable. In that case, a maximum  $\pm 10\%$  variation was permitted in the optimization process on  $\Omega$ . This slightly modified optimization problem is denoted  $\mathcal{T}\Omega$ . These two optimizations were conducted with the ABFM-QNC capabilities, using the optimization framework of pyOpt [30] and its SLSQP optimizer implementation. Optimizations have been conducted with an upper limit of 30 iterations. The QoI history is given in Figure 10 for each optimization problem. For both optimizations, the constraints were rigorously respected by the optimizer, resulting in a notable reduction of approximately 5% in compressor power consumption, with a gain slightly higher for  $\mathcal{T}\Omega$  than for  $\mathcal{T}$ , as expected from a larger design space. Both optimizations have reached the maximum number of iterations permitted. During the final  $\mathcal{T}$  optimization iterations, the variations in the objective function and constraints were minimal. The design variables also exhibited minimal variations for the final three optimization iterations (not shown in this document), indicating that the optimization process was almost converged. For the  $\mathcal{T}\Omega$  process, minor fluctuations in the QoIs, as well as in the design variables (not shown in this document), can be observed between iterations  $n^0$ 28 and 29.

## 4.1 Configurations comparison

The blade shape parameters associated with these optimized configurations are detailed in Table 1. For both optimized designs, the bounds imposed on the design variables have been reached for several design parameters, especially for rotor camber parameters at the leading edge in the upper half of the channel and at the trailing edge in the lower half of the channel. For the stator leading

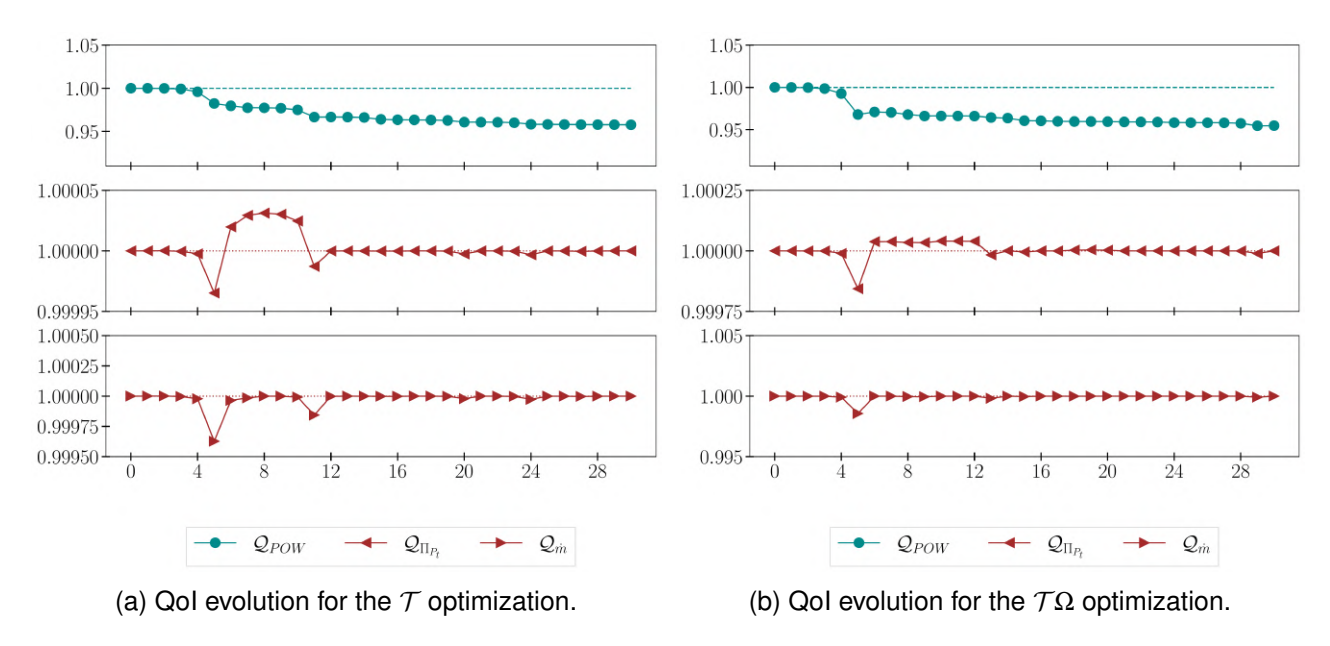


Figure 10 – Qol evolution for the two CME2 stage optimizations undertaken under radial inlet distortion.

edge, control point bounds at 50% and 75% channel height were found limiting to further improve the compressor performances.

For the  $\mathcal{T}$  optimized configuration, a notable increase in camber is observed at the rotor leading edge at 10% channel height<sup>1</sup>. Above, the rotor leading edge camber was lowered, with the amplitude of this reduction increasing with the channel height. This modification of the leading edge camber is consistent with the radial inlet distortion, which features a lower axial flow velocity at the bottom of the channel, resulting in an increased incidence on the blade. At the trailing edge, the modification is less smooth, as a strong decrease in camber is observed in the lower half of the channel, and a moderate one in the upper half. Consequently, the rotor camber is lowered over the entire blade, predominantly in the lower part of the channel. Similarly to the modifications of the rotor leading edge, the camber at the stator leading edge has been slightly increased at 10% channel height and gradually decreased at higher channel height. The maximum camber reduction was observed at h = 75%, and has reached the lower limit of the parameter range. These blade shape modifications are illustrated in Figures 11a to 11c.

The  $\mathcal{T}\Omega$  optimized configuration features a 1.3% decrease in rotor rotational speed. The shape deformations are very similar to those observed for  $\mathcal{T}$ . However, it can be noticed that the reduction in camber at the leading edge is more important than in the previous optimization. The maximum authorized camber deformation of  $-3^\circ$  is reached by  $\beta_{h50m0}^{rotor}$ ,  $\beta_{h75m0}^{rotor}$  and  $\beta_{h90m0}^{rotor}$ , while  $\beta_{h25m0}^{rotor}$  reaches 2.33°. In comparison, the same design variable reached only 0.42° in the previous optimization. A slight increase in camber is also observed at the rotor leading edge for this design, at 10% channel height, although this is of a much lower magnitude than in the  $\mathcal T$  optimization. These tendencies could have been anticipated since the reduction of the rotor rotational speed requires a re-alignment of the rotor blade to the incoming flow. Since the rotor rotation has been decreased but the total pressure ratio must remain constant, the rotor camber cannot be reduced as drastically as in the  $\mathcal T$  optimization. This explains why, although the deformation pattern of the rotor trailing edge in this optimization is similar to that in  $\mathcal T$ , the amplitude of the camber reduction is significantly lower.

Finally, it can be conjectured that the bounds imposed on the camber control points, which were reached for many design variables, have limited the optimizer ability to reduce the compressor rotational speed. In order to achieve further gains, it would be necessary to expand the range of variation of these variables and thus enhance the robustness of the body-force mesh deformation

<sup>&</sup>lt;sup>1</sup>For the blade shape parameterization software used in this study, a positive value of the  $\beta_{hX,mY}^{row}$  parameter means a reduction of the local camber at the rotor leading edge, and an increase of the local camber at both the rotor trailing edge and the stator leading edge.

Conf	Bounds	Baseline	$\tau$	$\mathcal{T}\Omega$		
Variable		Dounus	Daseille	,	/ 52	
	$\beta_{h10,m0}$			-1.39	-0.55	
	$\beta_{h25,m0}$			0.42	2.33	
Rotor leading edge	$\beta_{h50,m0}$	$[-3^{\circ}; +3^{\circ}]$	0.0	2.55	3.0	
	$\beta_{h75,m0}$			3.0	3.0	
	$\beta_{h90,m0}$			3.0	3.0	
	$\beta_{h10,m100}$			-3.0	-3.0	
	$\beta_{h25,m100}$			-3.0	-1.22	
Rotor trailing edge	$\beta_{h50,m100}$	$[-3^{\circ}; +3^{\circ}]$	0.0	-3.0	-1.27	
	$\beta_{h75,m100}$			-0.22	0.02	
	$\beta_{h90,m100}$			-0.80	-0.41	
Rotor rotating speed	$\Delta\Omega_a$	[-0.1; 0.1]	0.0	0.0	-0.013	
	$\beta_{h10,m0}$			0.03	-0.83	
	$\beta_{h25,m0}$			-0.97	-2.81	
Stator leading edge	$\beta_{h50,m0}$	$[-3^{\circ}; +3^{\circ}]$	0.0	-2.55	-3.0	
	$\beta_{h75,m0}$			-3.0	-3.0	
	$\beta_{h90,m0}$			-2.07	-2.81	

Table 1 –  $\mathcal{T}$  and  $\mathcal{T}\Omega$  optimized configuration parameters. All values are given in degrees, except for the non-dimensional rotating speed increment  $\Delta\Omega_a$ . Bold values correspond to the variables that have reached the optimization bounds.

process, that is currently the bottleneck.

A more quantitative comparison of the blade geometries can be undertaken through the analysis of the pitch law  $(\sigma)$  of each configuration. The results of this analysis are presented in Figure 12, with a comparison of the rotor and stator pitch angle along the channel height. Results for the  $\mathcal{T}$  final configuration are drawn in violet, those for the baseline in black, and those in cyan correspond to the  $T\Omega$  optimized geometry. For the T geometry, an opposite variation of the rotor pitch is observed between the upper and lower parts of the channel: the rotor pitch amplitude is decreased by  $-1.7^{\circ}$  at 80% channel height, while increased by  $2.1^{\circ}$  at h = 10%, compared to the baseline. This deformation is smooth along h and null at mid-span. On the contrary,  $\mathcal{T}\Omega$  features the same pitch amplitude reduction than  $\mathcal{T}$ , but on a larger portion of the blade span, from h=25% to h=90%. A 1.4° increase in pitch amplitude is observed at h = 10%, which is lower than T, but lead to an abrupt variation of the blade pitch near h=20%. For the stator, the analysis confirms that the  $T\Omega$  configuration exhibits a higher reduction of the blade pitch over the entire channel height than the  $\mathcal T$  geometry. It is also interesting to observe that the  $\mathcal{T}\Omega$  optimization process has reproduced the linear variation of  $\sigma$  with respect to h between 20 and 90% channel height, with the same slope. Below h = 20%, the  $\sigma(h)$  slope observed for  $T\Omega$  is more comparable to T than to the baseline, and corresponds to the break in the rotor pitch law. This is the direct effect of the mostly uniform deformation of the stator leading edge prescribed by the optimizer above h = 25%, that is due to the bounds imposed on these design variables. Therefore, despite the similarities discussed earlier, significant differences in the pitch laws can be observed between  $\mathcal{T}$  and  $\mathcal{T}\Omega$ , suggesting a different underlying trade-off conducted by the optimizer and therefore a different effect of the design variable bounds on the optimized geometry. Furthermore, these results also suggests that the ABFM is capable of adjusting the stator shape in accordance with the prescribed rotor deformations, as evidenced by the correlation observed between the variations in the pitch laws of both blade rows, for the two optimized configurations. Additionally, the reduction of the stator camber at its leading edge, observed for both

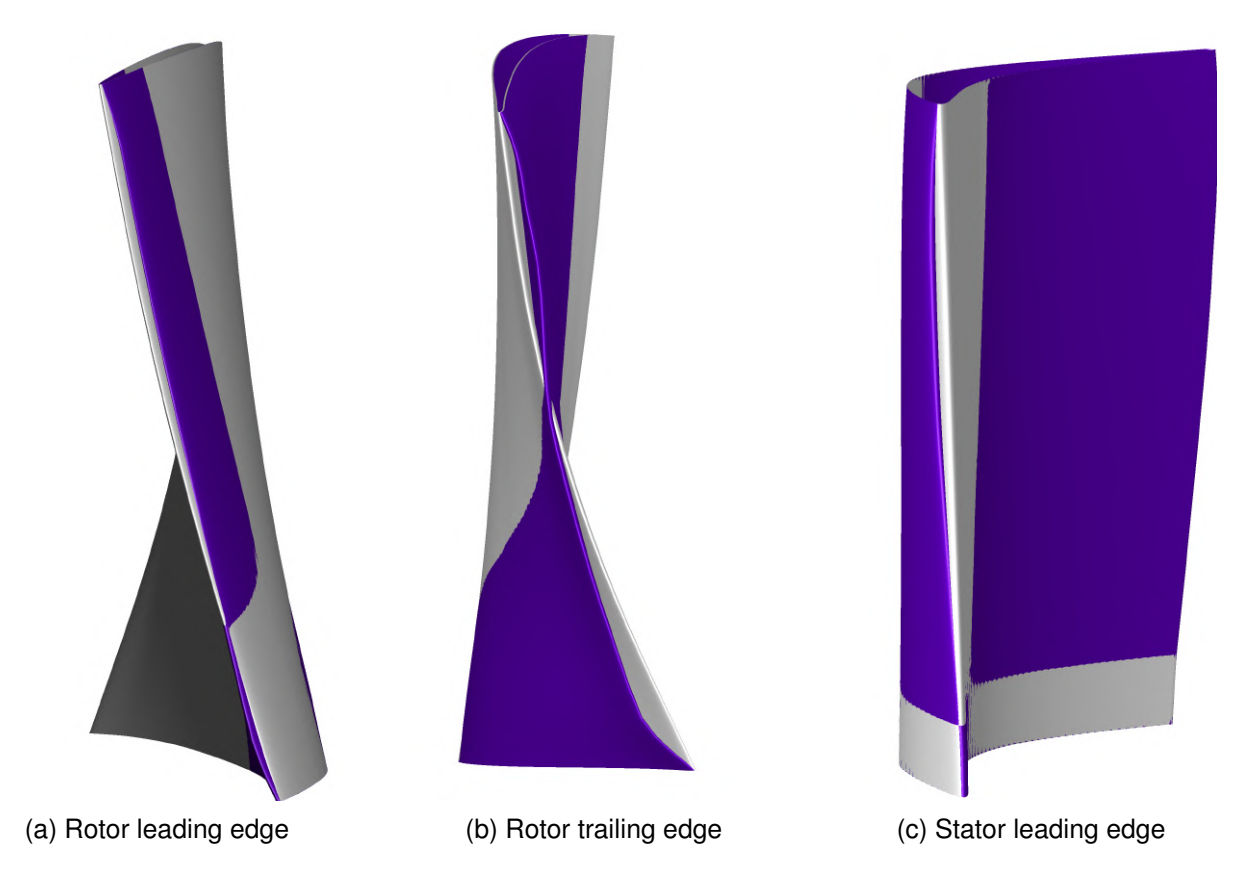


Figure 11 – Comparison of the rotor and the stator geometry, between the baseline configuration (in gray) and the optimized configuration (in violet) for the  $\mathcal{T}$  optimization.

optimized configurations, is found to be consistent with the expected overall reduction in swirl at the rotor exit for both optimized configurations. However, as illustrated in Figure 13 which depicts the radial profiles of the tangential flow velocity in the absolute frame of reference downstream of the rotor,  $\mathcal T$  exhibits a more pronounced reduction in swirl than  $\mathcal T\Omega$ , in comparison to the baseline. Consequently, according to the velocity triangle,  $\mathcal T$  should also display a greater reduction in camber at the stator leading edge than  $\mathcal T\Omega$ , in contrast to the comparison presented in Table 1. This discrepancy may prove to be another indication of a limited precision of the ABFM gradients for the stator, as previously postulated.

## 4.2 Comparative performance analysis

The performance metrics of the optimized configurations are now compared to those of the baseline. In Figure 14, the performances of the baseline  $\mathcal{B}$  are placed on the engine characteristics. The blade-resolved simulations are designated with the subscripts  $\bullet_{bladed}$ , while body-force simulations are identified with the subscript  $\bullet_{QNC}$ .

A comparison of the body-force performances of the baseline  $\mathcal{B}_{QNC}$  and the optimized configuration  $\mathcal{T}_{QNC}$  reveals a significant enhancement of the compressor isentropic efficiency at identical massflow-rate and compression ratio. A blade-resolved evaluation of the compressor performances, noted  $\mathcal{T}_{bladed}$ , at the same massflow-rate as the baseline reveals indeed an increase in isentropic efficiency, despite a notable decrease in total pressure ratio.

To accurately compare the performances of the optimized configuration against the baseline, the rotor rotation speed is gradually increased in the blade-resolved simulations until the desired total pressure ratio is achieved, while maintaining the baseline massflow-rate in the channel. The resulting configuration has a rotor rotation speed of 6475 RPM, representing an increase of 1.17% compared to the baseline. This novel configuration, designated  $\mathcal{T}_{bladed}^{6475\,\mathrm{RPM}}$ , exhibits a massflow-rate and total pressure ratio comparable to those of the baseline configuration,  $\mathcal{B}_{bladed}$ , while showing a notable enhancement in isentropic efficiency. A detailed comparison of the performances is presented in Table 2.

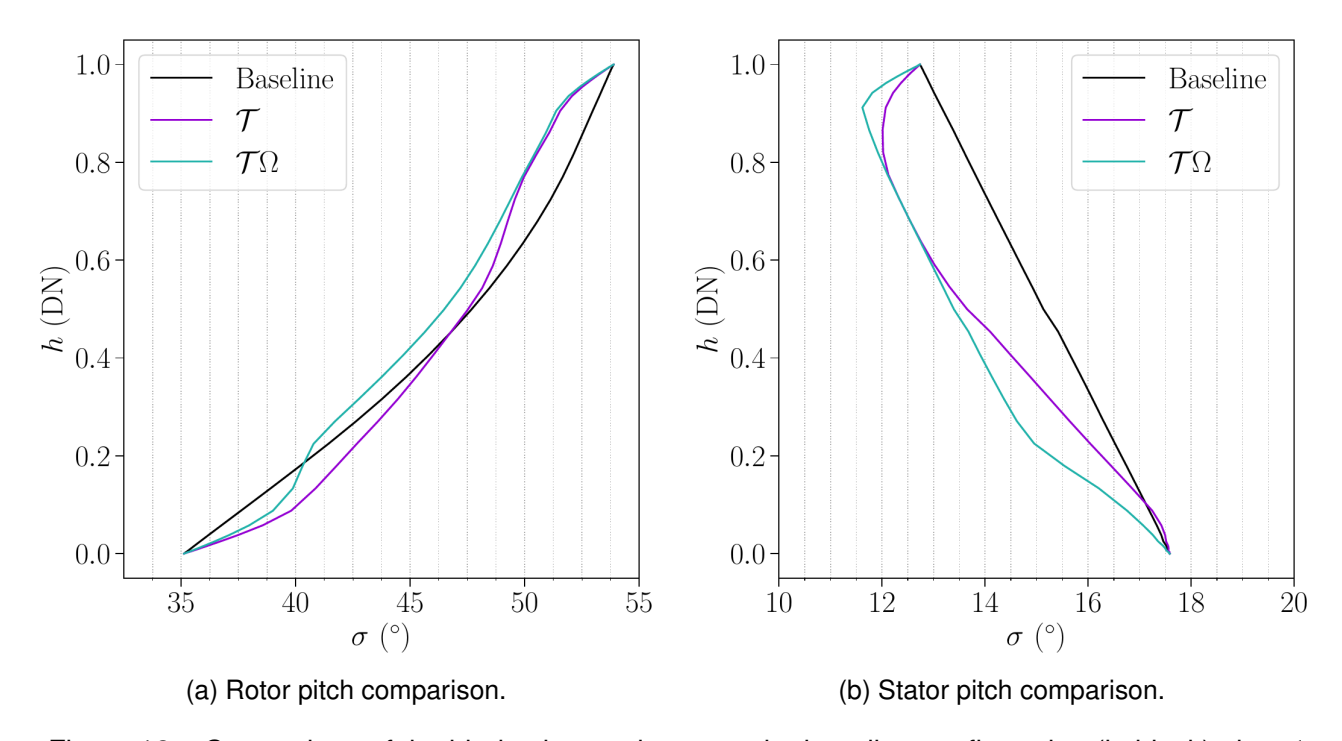


Figure 12 – Comparison of the blade shapes, between the baseline configuration (in black), the  $\mathcal{T}$  configuration (violet) and the  $\mathcal{T}\Omega$  optimized geometry (in cyan), for the rotor (a) and the stator (b). The blade pitch is drawn with respect to the non-dimensional channel height (h) for each row.

Qol		Bladed					BFM		
		$\mathcal{B}_{bladed}$	$\mathcal{T}_{bladed}$	delta	$\mathcal{T}_{bladed}^{6475 ext{RPM}}$	delta	$\mathcal{B}_{QNC}$	$\mathcal{T}_{QNC}$	delta
$Q_{\dot{m}}$	$\left(kg.s^{-1}\right)$	11.993	12.006	0.11%	11.993	0.00%	12.006	12.006	0.00%
η	(DN)	0.864	0.868	0.48%	0.874	1.16%	0.690	0.722	4.65%
$\mathcal{Q}_{POW}$	(W)	1.293 10 <sup>5</sup>	$1.22110^5$	-5.56%	1.278 10 <sup>5</sup>	-1.15%	1.326 10 <sup>5</sup>	$1.27010^5$	-4.23%
$\mathcal{Q}_{\Pi_{P_t}}$	(DN)	1.1158	1.1094	-0.58%	1.1157	-0.02%	1.0690	1.0690	0.00%

Table 2 – Comparison of performances between the baseline and the optimized configuration, using both body-force and bladed simulations, for the  $\mathcal{T}$  optimization geometry.

Without an increase in the rotor rotational speed, the blade-resolved simulation  $\mathcal{T}_{bladed}$  exhibits a mere 0.48% enhancement in compressor isentropic efficiency, despite a significant 5.56% reduction in power consumption. This reduction in power consumption is comparable to the -4.23% drop predicted by the body-force model for  $\mathcal{T}_{QNC}$ . However,  $\mathcal{T}_{bladed}$  features a significant decrease in total pressure ratio of -0.58%, which explains the modest gain in efficiency observed. With a higher rotational speed and therefore a nearly identical total pressure ratio to that of the baseline simulation,  $\mathcal{T}_{bladed}^{6475\text{RPM}}$  still exhibits an isentropic efficiency improvement far smaller than the one predicted by the body-force model. Nevertheless, this 1.16% increase in efficiency – which corresponds to a 1.0 percentage point (pp) gain – is still noteworthy and demonstrates that the ABFM-driven optimization has successfully adapted the compressor shape to the inlet distortion.

The performance metrics of the  $\mathcal{T}\Omega$  optimized configuration are also compared to the baseline in Table 3, using once again both BFM and blade-resolved simulations for this analysis. As observed for  $\mathcal{T}$ , the optimized configuration – with a reduced rotor rotational speed of  $6317\,\mathrm{RPM}$  – exhibits a significant decrease in power consumption, comparable to the one evaluated through body-force simulations, as well as a small increase in the compressor isentropic efficiency. However, the constraints on the massflow-rate and the total pressure ratio are not fully respected, with variations of the same amplitude as the gain observed on the isentropic efficiency. After enforcing the same massflow-

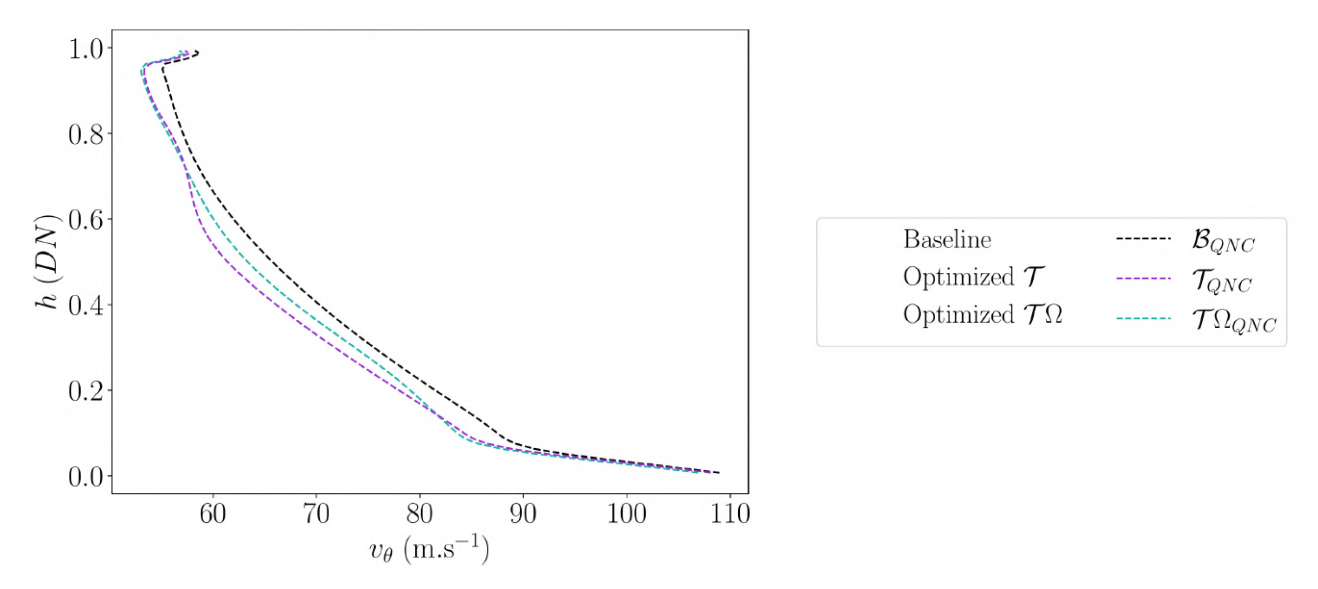


Figure 13 – Swirl levels downstream of the rotor in the absolute reference frame. Baseline BFM results are drawn in black,  $\mathcal{T}$  BFM results are drawn in violet and  $\mathcal{T}\Omega$  results are drawn in cyan.

rate in the single-blade passage channel, the rotor rotational speed was increased to 6375 RPM to obtain the same total pressure ratio than the baseline. The resulting configuration, designated  $\mathcal{T}\Omega_{bladed}^{6375\text{RPM}}$ , exhibits a 1.47% enhancement in the compressor isentropic efficiency and a -2.01% reduction in the power consumption. These gains are more pronounced than those observed in the previously optimized configuration  $\mathcal{T}_{bladed}^{6475\text{RPM}}$ , with a further 0.31% improvement in isentropic efficiency and an additional 0.86% reduction in power consumption. It was anticipated that the enlarged design space, which included the rotor rotational speed as a variable, would result in enhanced performance. However, the constraint on the total pressure ratio is less accurately satisfied for  $\mathcal{T}\Omega_{bladed}^{6375\text{RPM}}$  than for  $\mathcal{T}_{bladed}^{6475\text{RPM}}$ , which may introduce a small bias in the comparison.

Qol		Bladed					BFM		
		$\mathcal{B}_{bladed}$	$\mathcal{T}\Omega_{bladed}$	delta	$\mathcal{T}\Omega_{bladed}^{6375 ext{RPM}}$	delta	$\mathcal{B}_{QNC}$	$\mathcal{T}\Omega_{QNC}$	delta
$Q_{\dot{m}}$	$\left(kg.s^{-1}\right)$	11.993	12.030	0.31%	11.994	0.01%	12.006	12.006	0.00%
η	(DN)	0.864	0.872	0.84%	0.877	1.47%	0.690	0.724	4.97%
$\mathcal{Q}_{POW}$	(W)	1.293 10 <sup>5</sup>	$1.22110^5$	-5.58%	1.267 10 <sup>5</sup>	-2.01%	1.326 10 <sup>5</sup>	1.266 10 <sup>5</sup>	-4.53%
$\mathcal{Q}_{\Pi_{P_t}}$	(DN)	1.1158	1.1096	-0.56%	1.1151	-0.07%	1.0690	1.0690	0.00%

Table 3 – Comparison of performances between the baseline and the optimized configuration, using both body-force and bladed simulations, for the  $\mathcal{T}\Omega$  optimized geometry.

Between these two configurations, the rotor rotational speed is reduced from 6475 RPM to 6375 RPM, representing a decrease of 1.54%. This is similar to the decrease in rotor rotational speed predicted by body-force simulations between  $\mathcal{T}_{QNC}$  and  $\mathcal{T}_{QNC}$  (-1.3%). The difference in efficiency gain between  $\mathcal{T}_{\Omega_{QNC}}^{QCR6375RPM}$  and  $\mathcal{T}_{bladed}^{QCR6475RPM}$  on the one hand, and between  $\mathcal{T}_{\Omega_{QNC}}$  and  $\mathcal{T}_{QNC}^{QCR}$  on the other hand is also very similar (+0.3 pp against +0.2 pp). This demonstrates that the body-force is capable of capturing the design trends associated with the rotor rotation speed, despite the remaining limitations to precisely respect the  $\dot{m}$  and  $\Pi_{P_i}$  constraints. This information is highly encouraging, particularly in the perspective of aero-propulsive optimization of airframe layouts using the Hall-QNC model to simulate the engine system. Indeed,  $\Omega_{BFM}$  could be used to easily modulate the rotor rotation speed through the body-force model, and hence the thrust provided by the engine system, in order to balance the changes in drag resulting from airframe shape variations. These demonstrations of compressor optimization suggest that the ABFM correctly captures the influence of the variation of the rotor rotational speed on the compressor performance trends. Consequently, it may be used as

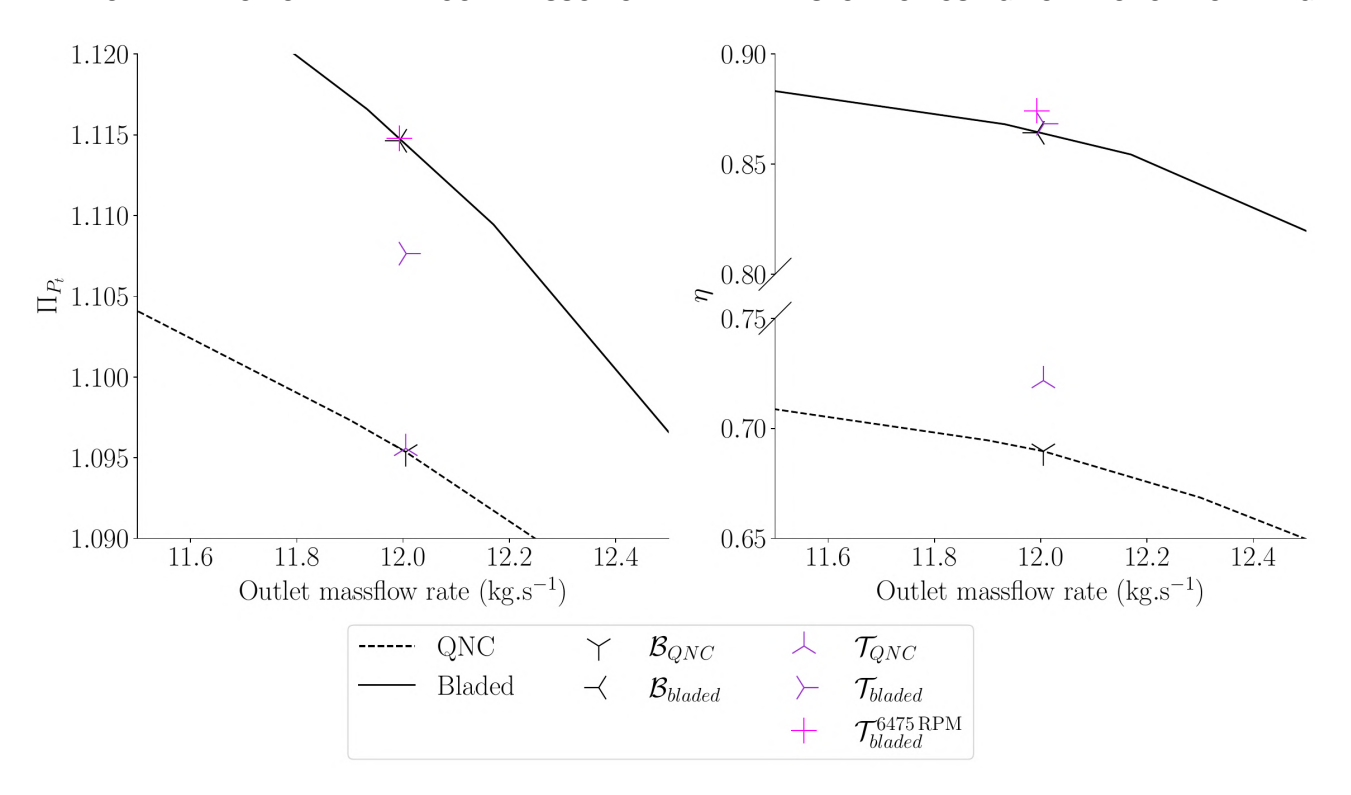


Figure 14 – Comparison of the optimized configuration performances against the baseline, placed on the baseline compressor characteristics drawn in plain lines, for the  $\mathcal{T}$  optimization.

a design variable in an aero-propulsive optimization.

Figure 15 compares radial profiles downstream of each blade row, for the three configurations under study. Baseline profiles are drawn in black dotted lines for  $\mathcal{B}_{ONC}$  and in black plain lines for  $\mathcal{B}_{bladed}$ . The  $\mathcal{T}$  optimized profiles are depicted in violet dotted lines for the body-force simulations ( $\mathcal{T}_{ONC}$ ) and in yellow plain lines for the blade-resolved simulation at  $\Omega = 6475$  RPM ( $\mathcal{T}_{bladed}^{6475}$ RPM). Finally, the  $\mathcal{T}\Omega$  optimized profiles are depicted in cyan dotted lines for the body-force simulations ( $\mathcal{T}\Omega_{ONC}$ ) and in green plain lines for the blade-resolved simulation at  $\Omega=6375\, RPM$  ( $\mathcal{T}\Omega_{bladed}^{6375\, RPM}$ ). On the total pressure ratio profiles, given in Figure 15a, we can observe that, for both optimized configurations, the rotor work has been decreased between 0 and 60% channel height, and increased above that limit. Consequently, the isentropic efficiency is decreased below  $h \approx 60\%$  and increased above. This results in an overall reduction of the total pressure transmitted by the rotor to the fluid, with a higher portion generated at the rotor tip, at higher isentropic efficiency. The body-force and blade-resolved results are in agreement on the tendency, although the first overestimates the amplitude of this change compared to the latter. Comparing both optimization results also reveals that the rotor work increase above h = 60% is reduced for  $T\Omega$  in comparison to T. On the contrary,  $T\Omega$  shows a lower reduction of the rotor work than  $\mathcal{T}$  for h between 20 and 60%. This indicates that both optimizations exhibit similar work redistribution over the rotor blade, but with a smaller amplitude for  $\mathcal{T}\Omega$  due to the reduction in rotational speed and the associated blade deformations. The body-force is capable to capture these tendencies with a very good accuracy, despite the remaining offset on the total pressure ratio. For the stator, a reduction in the total pressure losses is observed for both optimized geometries on blade-resolved contours between 0 and 80% channel height, with the greatest reduction occurring near  $h \approx 60\%$ . However, in the last 10% of the channel height, the total pressure losses are slightly increased.  $T\Omega$  reveals higher gain in the lower parts of the stator row, as well as lower losses near the shroud. This reduction in the total pressure losses compensates for the reduction in the rotor work observed earlier, and also explain part of the difference in power consumption between the  $\mathcal T$  and  $\mathcal T\Omega$  configurations. Once again, the body-force proves capable to capture this reduction of total pressure losses on the stator, even though it overestimates its amplitude and cannot capture the slight loss increase near the shroud. This may be explained by the absence of the rotor tip gap

leakage in the body-force simulation, which affects this region.

The observation of the entropy profiles, given in Figure 15b, confirms a reduction of entropy levels through the rotor for both optimized configurations for channel height above  $h \approx 30\%$ . While  $\mathcal T$  features a small but noticeable increase in entropy below this limit,  $\mathcal T\Omega$  exhibits a reduction of the entropy jump through the rotor for all channel heights, and shows higher gains than  $\mathcal T$  above h=30%. The BFM correctly predicts the higher efficiency gains for  $\mathcal T\Omega$  compared to  $\mathcal T$  in the lower part of the rotor row, however it also predicted slightly higher gains for  $\mathcal T$  at mid-span, which is not observed on the blade-resolved simulations.

In the radial profiles of entropy variation through the stator row, the  $\mathcal{T}\Omega$  configuration exhibits a significant reduction in entropy at all channel high, of higher amplitude than  $\mathcal{T}$ . For the latter, the gains are mostly observed above h=20%. For both optimized configurations, the largest reduction in entropy levels are observed the the middle of the channel. Once again, the gains predicted by the body-force simulation show similar trends but are overestimated. This shows that not only has the ABFM proved capable of adapting the shape of the stator in line with the deformations imposed on the rotor, it has also improved its performance, i.e. reduced its total pressure losses and entropy levels. It suggest once again that, even though certainly not as accurate as for the rotor, the ABFM stator gradients must be relevant for stage shape optimizations.

In addition, as already noticed on the total pressure radial profiles, the body-force model predicts significantly higher entropy gains for the  $\mathcal{T}\Omega$  configuration than for  $\mathcal{T}$  at high channel heights on the stator row, that are not observed on blade-resolved simulations. Once more, the BFM appears to have failed to account for a crucial flow feature at this location, which drives the losses. This feature is likely the interaction between the stator and the rotor tip-gap vortex. Elsewhere, the discrepancy in the predicted gains may be attributed to the overestimation of the losses by the QNC body-force model. Indeed, this also leads to an overestimation of the gains offered by the modifications of the blade shapes. A proper treatment of the calibration process of the Hall-Thollet model in the gradient assembly and in the optimization chain might therefore help mitigate these limitations. This calibration, however, necessitates a greater number of primal BFM simulations required for each design investigated during the optimization process, and also to a more complex gradient assembly if the sensitivities with respect to the blade shape parameters through the calibration process are to be taken into account.

## 5. Conclusion and perspectives

This study applies the novel Adjoint Body-Force Modeling (ABFM) methodology, presented and validated in a previous contribution, to the design of an axial compressor subject to radial inflow distortions. First, a gradient comparison study demonstrated that the ABFM remains capable of accurately predicting the gradients of the performance metrics necessary to conduct a stage design-optimization under inlet distortions, at design massflow-rate as well as close to the stability limit. As observed in the authors' previous study, these capabilities are, however, reduced near the choke since no blockage modeling has yet been implemented in the implemented ABFM library. If the ABFM stator gradients prediction accuracy cannot yet be discussed in details, it already appears rather limited. At best, the ABFM may prove capable of predicting the correct sign and order of magnitude of most of the stator shape gradients, which remains sufficient for the ABFM-driven shape optimization to correctly adapt the stator shape to the rotor deformations.

This novel tool was then applied to perform two compressor adjoint-based optimizations, with and without the rotor rotation speed serving as a design variable. These proof-of-concept optimizations resulted in an increase in stage efficiency from 1 to 1.2 percentage points, despite the potential lack of structural soundness in the obtained geometries. Blade-resolved analyses indicated that the ABFM-driven shape optimization was capable of adapting the stator shape accordingly to the rotor shape deformations, and was also found capable to slightly increase its performance. A comparison of the radial profiles for the various configurations obtained from both blade-resolved and BFM simulations demonstrated that the body-force was capable of capturing the correct location of the efficiency gains obtained through the optimization, even for rather subtle differences between the two optimized configurations. Despite the limitations intrinsic to the simplified model and the BFM itself, this demonstrates that the ABFM is a highly promising tool for the efficient design optimization of compressors.

The capacity of this model to accurately capture the sensitivity of compressor performance metrics with respect to blade shape parameters and rotation speed under inlet distortion is highly encouraging in the context of using this tool for the optimization of tightly integrated aero-propulsive configurations. This paves the way towards the simultaneous optimization of both the airframe and the fan geometry. The current studies are focused on extending the ABFM application to the optimization of axial compressors under full-annulus BLI-like inlet distortions. Concurrently, a comparison between blade-resolved and ABFM adjoint-based optimization is being conducted to compare the different stage configurations obtained with each method, as well as the efficiency gains offered by each optimized configuration. Finally, further investigations are being conducted on ABFM stator shape gradients to provide an accurate evaluation of the relevance of these gradients. Further work will entail enhancing the fidelity of the Hall-Thollet body-force model incorporated into the ABFM library and improving the numerical robustness of the ABFM optimization process, in order to facilitate the application of this tool to aero-propulsive design studies.

## 6. Acknowledgments

This work is supported by the European project NEXTAIR which has received funding from the European Union's Horizon Europe research and innovation program under grant agreement No 101056732. Views and opinions expressed are however those of the authors only and do not necessarily reflect those of the European Union. Neither the European Union nor the granting authority can be held responsible for them.

## 7. Copyright Statement

The authors confirm that they, and/or their company or organization, hold copyright on all of the original material included in this paper. The authors also confirm that they have obtained permission, from the copyright holder of any third party material included in this paper, to publish it as part of their paper. The authors confirm that they give permission, or have obtained permission from the copyright holder of this paper, for the publication and distribution of this paper as part of the ICAS proceedings or as individual off-prints from the proceedings.

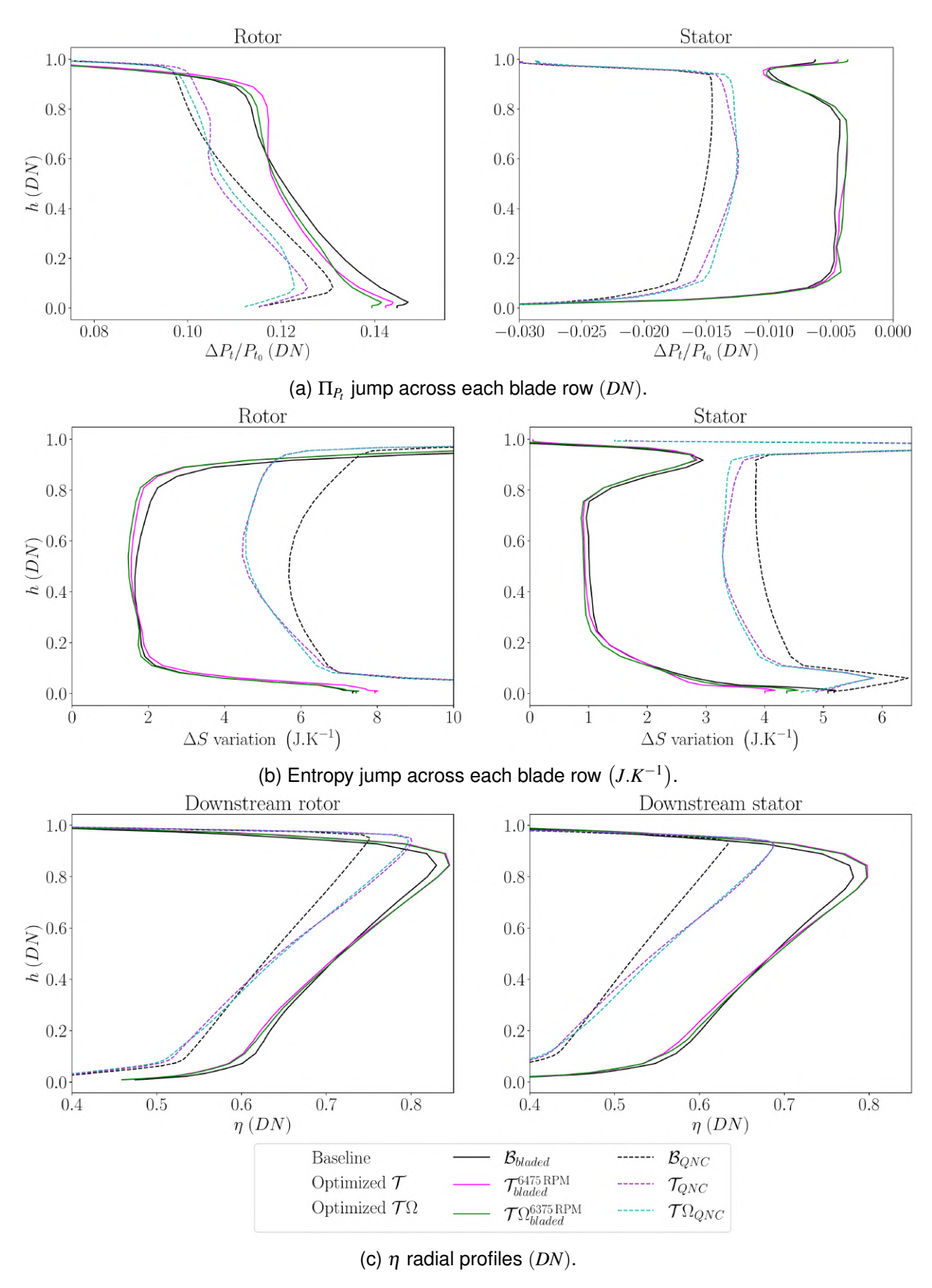


Figure 15 – Radial profiles of total pressure ratio (a) and of the entropy variation (b) increase across each row, and of the isentropic efficiency downstream of each row (c) for the  $\mathcal{T}$  (in yellow for the blade-resolved results at 6475 RPM and in violet for BFM results) and the  $\mathcal{T}\Omega$  (in green for blade-resolved results at 6375 RPM and in blue for BFM results) compressor optimizations under radial inlet distortion. Variations across the rotor (respectively, the stator) were evaluated by comparing the flow state between stations B and A (respectively, C and B). The isentropic efficiency is measured downstream of the rotor (respectively the stator) at station B (respectively, C). 23

#### References

- [1] Gregg G. Fleming and Ivan de Lépinay. Environmental trends in aviation to 2050. Technical Report Chapter One, ICAO, 2016.
- [2] International Air Transport Association. Working Towards Ambitious Targets.
- [3] Marc Borel and Béatrice Vinstock. Aviation & changement climatique. Technical report, Direction Générale de l'Aviation Civile, March 2018.
- [4] Benjamin Godard, Nabil Ben Nasr, Raphaël Barrier, Julien Marty, Nicolas Gourdain, and Edouard De Jaeghere. Methodologies for Turbofan Inlet Aerodynamics Prediction. In *35th AIAA Applied Aerodynamics Conference*, Denver, Colorado, June 2017. American Institute of Aeronautics and Astronautics.
- [5] William Thollet, Guillaume Dufour, Xavier Carbonneau, and Florian Blanc. Assessment of body-force methodologies for the analysis of intake–fan aerodynamic interactions. *American Society of Mechanical Engineers*, page 9, 2016.
- [6] Andreas Peters, Zoltan S. Spakovszky, Becky Rose, and Wesley K. Lord. Ultra-Short Nacelles for Low Fan Pressure Ratio Propulsors. *American Society of Mechanical Engineers*, page 15, 2014.
- [7] Benjamin Godard, Edouard De Jaeghere, and Nicolas Gourdain. Efficient Design Investigation of a Turbofan in Distorted Inlet Conditions. In *Volume 2A: Turbomachinery*, page V02AT39A011, Phoenix, Arizona, USA, June 2019. American Society of Mechanical Engineers.
- [8] Alan Burlot, Fulvio Sartor, Maxime Vergez, Michaël Méheut, and Raphaël Barrier. Method Comparison for Fan Performance in Short Intake Nacelle. In *2018 Applied Aerodynamics Conference*, Atlanta, Georgia, June 2018. American Institute of Aeronautics and Astronautics.
- [9] Sebastian Spinner, Marco Trost, and Rainer Schnell. An Overview of High Fidelity CFD Engine Modeling. In *AIAA SCITECH 2022 Forum*, San Diego, California, United States of America, January 2022. American Institute of Aeronautics and Astronautics. https://arc.aiaa.org/doi/pdf/10.2514/6.2022-0430.
- [10] Luis López de Vega, Dufour Guillaume, and Garcias Rosa Nicolas. Fully Coupled Body Force–Engine Performance Methodology for Boundary Layer Ingestion. *Journal of Propulsion and Power*, 37(2), April 2021.
- [11] Li Da, Lu Hanan, Yang Zhe, Pan Tianyu, Du Hai, and Li Qiushi. Optimization of a transonic axial-flow compressor under inlet total pressure distortion to enhance a. *Engineering Applications of Computational Fluid Mechanics*, page 21, June 2020.
- [12] Sandeep Kumar, Mark G. Turner, and Mark L. Celestina. Non-Axisymmetric Design-Optimization of Inlet Guide Vanes for a Fan with Inlet Distortion. In *GPPS Chania20*, page 10, Chania, Greece, September 2020.
- [13] David K. Hall. Analysis of civil aircraft propulsors with boundary layer ingestion. PhD Thesis, MIT, 2015.
- [14] William Thollet. Modélisations simplifiées de turbomachines pour l'analyse par la simulation des installations motrices complexes d'avions/Body force modeling of fan-airframe interactions. PhD Thesis, Université de Toulouse, July 2017.
- [15] Cyril Dosne, Raphaël Barrier, Sébastien Bourasseau, Marco Carini, Rocco Moretti, and Jacques Peter. A First Assessment of Adjoint Body-Force Modeling Capabilities for Fan Design. In *AIAA SCITECH 2024 Forum*, Orlando, Forida, United States of America, January 2024. American Institute of Aeronautics and Astronautics. https://arc.aiaa.org/doi/pdf/10.2514/6.2024-2640.
- [16] Frank E. Marble. Three dimensional Flow in Turbomachines. In *Aerodynamics of turbines and compressors*, volume X of *High Speed Aerodynamics and Jet Propulsion*, pages 83–166. Princeton, New Jersey, United States of America, princeton university press edition, 1964.
- [17] Cyril Dosne, Raphaël Barrier, Sébastien Bourasseau, Marco Carini, Rocco Moretti, and Jacques Peter. An Adjoint Body-Force Approach for Fully-Coupled Aero-propulsive Optimizations. In EUROGEN 2023: 15th International Conference on Evolutionary and Deterministic Methods for Design, Optimization and Control, Chania, Greece, June 2023. ECCOMAS Proceedia. https://doi.org/10.7712/140123.10197.18932.
- [18] Benjamin Godard. Étude et méthodologies de simulation de doublet entrée d'air soufflante pour la conception de turbofan de nouvelle génération. PhD Thesis, Université de Toulouse, 2018.
- [19] Bruno Maugars, Sébastien Bourasseau, Cédric Content, Bertrand Michel, Bérenger Berthoul, Jorge Nunez Ramirez, Pascal Raud, and Laurent Hascoët. Algorithmic Differentiation for an efficient CFD solver. In *ECCOMAS 2022 8th European Congress on Computational Methods in Applied Sciences and Engineering*, page 22, Oslo, Norway, June 2022.
- [20] Laurent Cambier, Sébastien Heib, and Sylvie Plot. The Onera *elsA* CFD software: input from research and feedback from industry. *Mechanics & Industry*, 14(3):159–174, 2013.
- [21] Julien Marty, Lionel Castillon, and Pierric Joseph. Numerical Investigations on the Rotating Stall in an

- Axial Compressor and Its Control by Flow Injection at Casing. *Journal of Turbomachinery*, 145(051009), November 2022.
- [22] Clémence Rannou. *Méthodologie pour la modélisation du contrôle actif d'écoulement dans un compresseur axial.* phdthesis, HESAM Université, November 2023.
- [23] Steven R. Allmaras, Forrester T. Johnson, and Philippe R. Spalart. Modifications and Clarifications for the Implementation of the Spalart-Allmaras Turbulence Model. *Computational Fluid Dynamics*, 2012.
- [24] Julien Dandois. Improvement of Corner Flow Prediction Using the Quadratic Constitutive Relation. *AIAA Journal*, 52(12):2795–2806, December 2014. https://arc.aiaa.org/doi/10.2514/1.J052976.
- [25] Philip L. Roe. Approximate Riemann solvers, parameter vectors, and difference schemes. *Journal of Computational Physics*, 43(2):357–372, October 1981.
- [26] Vincente J. Fidalgo, C A. Hall, and Y Colin. A Study of Fan-Distortion Interaction Within the NASA Rotor 67 Transonic Stage. *Journal of Turbomachinery*, page 12, May 2012.
- [27] Joaquim R. R. A. Martins. Aerodynamic design optimization: Challenges and perspectives. *Computers & Fluids*, 239:105391, May 2022.
- [28] Rodrick V. Chima. A Three-Dimensional Unsteady CFD Model of Compressor Stability. pages 1157–1168. American Society of Mechanical Engineers Digital Collection, May 2006.
- [29] Anjaney P. Kottapalli. Development of a Body Force Model for Centrifugal Compressors. Master's thesis, Massachusetts Institute of Technology, August 2013.
- [30] Ruben E. Perez, Peter W. Jansen, and Joaquim R. R. A. Martins. pyOpt: a Python-based object-oriented framework for nonlinear constrained optimization. *Structural and Multidisciplinary Optimization*, 45(1):101–118, January 2012.